Fundamental Studies of Diesel Particulate Filters: Transient Loading, Regeneration and Aging

Athanasios G. Konstandopoulos

Foundation for Research and Technology – Hellas/Chemical Process Engineering Research Institute (FORTH/CPERI); ME, EM Department, Michigan Technological University

Margaritis Kostoglou, Evangelos Skaperdas, Eleni Papaioannou, Dimitrios Zarvalis and Evdoxia Kladopoulou

Foundation for Research and Technology – Hellas/Chemical Process Engineering Research Institute (FORTH/CPERI)

**The Engineering Society
For Advancing Mobility
Land Sea Air and Space®
INTERNATIONAL**

GLOBAL MOBILITY DATABASE

All SAE papers, standards, and selected books are abstracted and indexed in the Global Mobility Database

Fundamental Studies of Diesel Particulate Filters: Transient Loading, Regeneration and Aging

Athanasios G. Konstandopoulos
Foundation for Research and Technology – Hellas/Chemical Process Engineering
Research Institute (FORTH/CPERI); ME, EM Department, Michigan Technological University

Margaritis Kostoglou, Evangelos Skaperdas, Eleni Papaioannou, Dimitrios Zarvalis and Evdoxia Kladopoulou
Foundation for Research and Technology – Hellas/Chemical
Process Engineering Research Institute (FORTH/CPERI)

ABSTRACT

Compliance with future emission standards for diesel powered vehicles is likely to require the deployment of emission control devices, such as particulate filters and DeNO$_x$ converters. Diesel emission control is merging with powertrain management and requires deep knowledge of emission control component behavior to perform effective system level integration and optimization. The present paper focuses on challenges associated with a critical component of diesel emission control systems, namely the diesel particulate filter (DPF), and provides a fundamental description of the transient filtration/loading, catalytic/NO$_2$-assisted regeneration and ash-induced aging behavior of DPF's. The derived models (some in analytic form) are based on rigorous descriptions of the underlying physicochemical processes and they are shown to be in excellent agreement with experimental data (collected in-house and from the literature) as well as by comparison to, "presumably exact", 3-dimensional Computational Fluid Dynamics calculations. The validated models thus provide a robust core to build upon/interface system level simulation and optimization tools.

INTRODUCTION

The global automotive industry is currently facing complex challenges to provide solutions that reduce transportation related environmental impact, conserve energy and advance social welfare without adverse effects on economic growth, employment and competitiveness. Significant reductions in CO$_2$ emissions and the associated greenhouse-related environmental impacts of internal combustion engines, can be effected through increased deployment of the modern, highly efficient, direct injection (DI) diesel engine. This requires that engine manufacturers meet increasingly tightened particulate matter (PM) and NO$_x$ emissions legislation [1-3]. The use of diesel particulate filter (DPF) systems (traps) appears inescapable for complying with heavy-duty engine emission standards in the next five years. The evolution of light-duty diesel emission standards is likely to make necessary the introduction of particulate emission control systems before the end of the decade, on both sides of the Atlantic [1]. Efficient DPF's can quickly accumulate significant amounts of particulates. These collected particles have to be removed from the filter by oxidation in order to prevent excessively high pressure drop in the exhaust system, which would affect the engine operation. The in-situ particulate oxidation process is termed regeneration of the filter. The availability of reliable, and efficient particulate reduction technology in combination with appropriate engine management/tuning and DeNO$_x$ technology, would then enable the diesel engine to become the automotive power plant of choice for the future.

It is becoming widely appreciated in the last years, that exhaust emission reduction devices should be an integral part of the powertrain. A shift in paradigm thus is becoming evident, from the "black-box converter" fitted to the exhaust of an already developed engine/vehicle, towards a framework of "concurrent engineering and integrated design" at the system level. This requires deep knowledge of emission control component behavior to perform effective system-level integration and optimization. A long-term research program carried out at the Aerosol & Particle Technology (APT) Laboratory of FORTH/CPERI is concerned with contributions to this framework, that would allow fast optimization of diesel emission control systems, as well as assist in the development of control strategies and assessment of novel concepts. In the present paper we discuss critical

aspects of the diesel particulate emission control, with emphasis on the fundamentals of the filtration/loading, regeneration and aging behavior of DPF's.

The structure of the paper is as follows. At first a brief review of DPF technology is given to set the stage for the subsequent developments. Then analytical and numerical models for the transient loading and filtration process of a wall-flow DPF are derived and validated with experimental data and CFD simulations for different filter materials. The regeneration behavior of DPF's is further studied extending a mathematical model, developed previously by the authors, to cover the combined influence of NO_2 and catalytic coatings on diesel particulate oxidation. The new model is validated against experimental data collected in a dedicated pilot-scale filter testing unit, connected to a diesel engine bench. Finally the aging process of the filter pressure drop due to ash accumulation is simulated and validated against experimental data from the literature.

REVIEW OF DPF TECHNOLOGIES

Filters separate the typically sub-µm diesel particulate from the exhaust with a variety of transport mechanisms. Main deposition mechanisms are those of Brownian diffusion and direct interception while thermophoresis can be important in the presence of temperature gradients [4]. In the last 15 years many DPF system concepts have appeared, incorporating different filter media and geometric configurations, regeneration technologies and control/monitoring options. The interested reader should consult the recent literature [1-3] as well as on-line databases [5]. Filter media and geometric configuration is a key element in the DPF system and the selection process deserves careful balancing of different criteria including pressure drop performance, particulate collection efficiency, ease of regeneration, durability and cost. A partial list of available commercially or as prototypes filter media is shown in Table 1.

Table 1. Available Media for Diesel Particulate Filters

Ceramic
  • Cordierite (extrudates)
  • Mullite (extrudates, foams, fibers, infiltrates)
  • Silicon Carbide (extrudates, foams, felts, infiltrates)
  • Tialite (extrudates)
  • Mullite/zirconia (extrudates, foams)
  • Mullite/tialite (extrudates, foams)

Metallic
  • Sintered metal
  • Wire mesh
  • Metal foam

Geometric configurations of filters are listed in Table 2 and some are schematically illustrated in Figure 1.

The wall-flow monolith honeycomb design originally introduced in 1981 [6] still remains the most popular configuration, since it exhibits a very compact arrangement, exhibiting thus a low pressure drop without sacrifice in filtration rate or available space.

Table 2. Geometric Configurations for DPF's

  • Extruded honeycomb wall-flow monoliths
  • Assembled parallel plate wall-flow elements
  • Cylindrical Cartridges (based on fibrous structures)
  • Foam monolithic blocks and plates
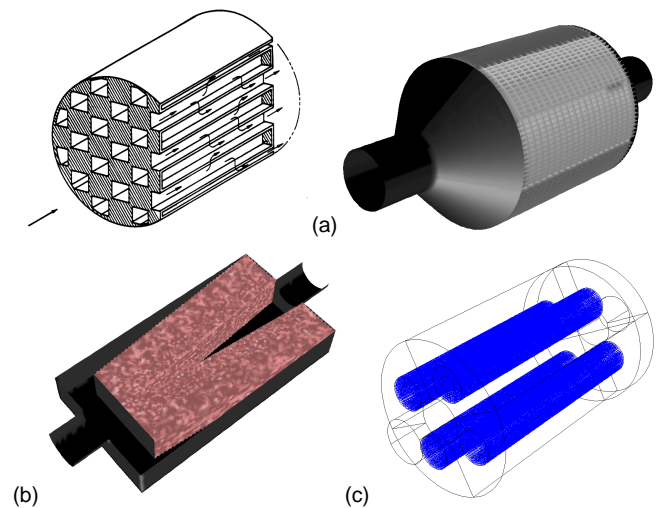 • Concentric tubular wall-flow elements

Figure 1.   Geometric configurations of some commercially available DPF's : (a) honeycomb wall-flow monolith, (b) V-shaped foam filter, and (c) cylindrical fibrous cartridge.

Since the majority of filter configurations uses some sort of wall-flow arrangement we will focus our investigation for the remaining of the paper on the wall-flow geometry and honeycomb structures. It should be noted though, that the developments/results can be extended straightforwardly to the other geometries.

Regeneration of diesel traps requires temperatures in excess of 550 °C. Such exhaust temperatures do not occur often in practical applications of the diesel engine. Especially in light-duty diesel applications the exhaust gas temperature can be as low as 100-200°C, for most of the driving route of the vehicle, especially in cities. Successful regeneration of diesel traps should achieve fast, reliable and cost effective conversion of the accumulated particulate mass, before the trap backpressure rises to unacceptably high levels.

It is convenient to classify regeneration measures [1-3,5] as active (employing external or engine means, see Table 3) or passive (usually employing catalytic means,

although catalytic means can also be applied in active systems, see Table 4). Combinations of measures are also common.

Table 3. Active Regeneration Measures

External means
- Fuel burners (full and partial flow)
- Electric heating (upstream or embedded in the filter)
- Micro-wave heating
- Injection of combustibles (e.g. fuel) in the exhaust
- Injection of catalytic and/or reactive species in the exhaust (e.g. H_2O_2 [7])
- Generation of reactive species (e.g. non-thermal plasma [8])
- Electrochemical filter reactor [9]

Engine means
- Exhaust gas recirculation
- Post-injection of fuel
- Decrease of boost pressure
- Intercooler by-pass
- Injection timing retard

Table 4. Passive Regeneration Measures

Catalytic means
- Fuel-borne catalysts
- Catalytic filter coatings
- Reactive species generation (e.g. NO_2 [10])

Effective catalytic oxidation of diesel particulate relies on the establishment of good contact between the soot particles and active catalyst sites [11], where oxidation takes place. Catalyzed diesel particulate filters involve the deposition of catalytic coatings on the filter media, while fuel-borne catalysts are continuously supplied with the fuel. Applications combining fuel-borne catalysts and catalytically coated filters have also been suggested [12]. The particulate oxidation mechanism with fuel catalytic additives is similar to that in a catalyzed trap. Commercially available regeneration promoting fuel-borne catalysts are based on Cerium (Ce), Copper (Cu), Iron (Fe), Platinum (Pt), Strontium (Sr) and Sodium (Na) fuel-soluble compounds and their combinations [1-3, 5]. In fleet operations, the catalytic compounds can be dopped in a central fuel tank, while for application to individual vehicles a reliable on-board, controlled dosing system is required. The combined use of a fuel-borne catalyst and temperature-raising engine measures, are employed in a recent particulate emission control system marketed by a European car manufacturer [13].

In other recent developments, diesel particulates are removed through oxidation by NO_2 [10]. Initially the technology required low-fuel sulphur content (<10 ppm), but it is believed that it can operate with up to 50 ppm sulphur content in the fuel, provided there is a favorable NO_x/C ratio in the engine out emissions.

Finally, non-thermal plasma based technologies [5] can be exploited to promote diesel particulate oxidation at low temperatures [8], through the creation of highly reactive species (including NO_2) and radicals. However, the actual potential of such technologies integrated with modern diesel engines remains to be systematically investigated and assessed against performance, reliability and cost (Table 5).

Table 5. Assessment Aspects for DPF Systems

Performance
- Filtration efficiency (mass, number, size-specific)
- Effects on other emissions
- Pressure drop at rated speed/full load (fresh, regeneration limit, safety limit)
- Regeneration efficiency
- Noise reduction

Reliability
- Monitoring, control and safety warning algorithms
- Life expectancy, aging performance
- Inspection and maintenance verification protocols

Cost
- Capital cost (including system integration, optimization and tampering resistance)
- Operating cost (including fuel penalty)
- Maintenance cost

In summary, diesel particulate filter regeneration technologies aim at increasing the reactivity of the accumulated carbonaceous particulate either by raising (directly or indirectly) the exhaust gas temperature, or by making the particulate and/or the environment in the filter intrinsically more reactive, or both. Lately, heat recovery approaches are under investigation for extending the operating range of regeneration strategies. These involve heat recovery by reciprocating flow operation [14] as well as through the use of heat recuperators [15].

It is convenient to distinguish between two regimes of DPF operation namely filtration/loading and regeneration. However for some technologies the boundary between these regimes can be blur or even non-existent (e.g. in continuously regenerating systems). In the following we study these two regimes.

FILTRATION AND LOADING BEHAVIOR

OVERVIEW OF THEORETICAL DEVELOPMENTS – The first applications and validations of filtration theory to diesel particulate filters were done in [16] for fibrous structures and in [4] for wall-flow extruded filters. In these studies it was shown that classic filtration theory employing the concept of the "unit collector" (spheres for extruded filters and cylinders for fiber and foamy

structures) can give a good estimate of the size-specific collection efficiency of "clean" DPF's with respect to solid particles. The first study that provided validated design equations for sizing wall-flow filters based on fundamental principles of fluid mechanics and flow through porous media (Darcy's law) was by Konstandopoulos and Johnson [4] using a one-dimensional (perimeter averaged) model of the trap channels. In that study analytical solutions were obtained for the flow fields and pressure drop of wall-flow monoliths in terms of the filter media microstructure and geometric configuration, that were validated experimentally for a particular extruded monolith design. The analytical model (extended for non-Darcian flow effects) was recently shown to be in excellent agreement with 3-D Computational Fluid Dynamics (CFD) simulations and was further validated against a larger variety of filter media [17]. Furthermore, explicit design and optimization criteria for a systematic selection of the filter material microstructural characteristics and filter configuration (wall thickness, cell density, length) were obtained, for routine sizing of wall-flow monoliths with special emphasis on filters regenerating continuously [17]. The Konstandopoulos and Johnson [4] model was very recently extensively tested against a variety of filter samples, and it is reported to give excellent *a priori* predictions of the pressure drop, opening new development possibilities [18,19].

Appendix I presents the extension of the Konstandopoulos et al. [4, 17] trap pressure drop model to the case of arbitrary filter loadings. An analytical expression derived for the trap pressure drop as a function of particulate loading (expressed in terms of a uniform, effective deposit thickness, *w* on the filter wall) is given below:

$$\Delta P = \frac{\mu Q}{2V_{trap}}(\alpha + w_s)^2\left[\frac{w_s}{k_o\alpha} + \frac{1}{2k_{soot}}ln\left(\frac{\alpha}{\alpha - 2w}\right) + \right.$$
$$\left. + \frac{4FL^2}{3}\left(\frac{1}{(\alpha - 2w)^4} + \frac{1}{\alpha^4}\right)\right]$$
(1)

The symbols appearing in Eq. (1) are defined in a separate section at the end of the paper.

For coated filters, temperature dependent slip-flow effects cause the pressure drop to deviate from the continuum form of Darcy's law, however these can be accounted as shown in Appendix II through a simple procedure, see also [4]. Figure 2 illustrates how the pressure drop dependence of a membrane-coated cordierite filter [20] is accurately described in terms of the slip-flow corrected permeability (Appendix II) that depends on the local value of the Knudsen number of the flow through the coating.
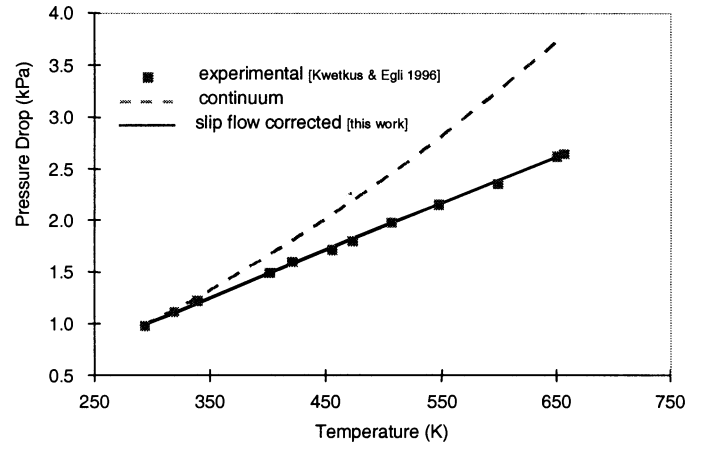

Figure 2. Effect of temperature on pressure drop of a membrane coated filter, experiment [20] and theory (see Appendix II for slip-flow corrected theory).

Depending on their microstructure, filters can exhibit a transition from the so-called deep bed filtration regime, to the cake (or surface) filtration regime [21], characterized by a linear dependence of the pressure drop on the accumulated particulate mass in the filter. DPF's are no exception and for some filters such behavior has been documented experimentally in the literature [22, 23]. In Appendix III we describe the extension of the clean filter model of Konstandopoulos and Johnson [4], based on the concept of the "unit collector", into the domain of transient filtration/loading. The derived model is based on first principles that describe the spatial deposition of particles inside the porous filter wall, and simulates in a natural way the deep-bed-to-cake transition through the progressive blocking of the filter wall. The model equations cannot be solved analytically, but a very efficient numerical code (*FilSim* v.1.0) has been developed for their solution. The transient filtration algorithm is shown in the flow chart of Figure 3 and is briefly described below.

A prescribed particle size distribution (particle size loop in Figure 3) is tracked through the filter medium, which is discretized in slabs where the local collection efficiency is computed using the concept of the "unit collector" (spatial efficiency loop in Figure 3). The locally deposited mass along the filter thickness modifies the microstructure (spatial microstructure loop in Figure 3) -porosity, collector diameter- of each slab which in turn determines the new local collection efficiency and pressure drop. The procedure is repeated for every time step (temporal loop in Figure 3) to compute the evolution of the filter behavior in terms of collection efficiency and pressure drop. Eventually a cake emerges from the wall, and deposit growth continuous on the surface of the filter cake.

The *FilSim* code can accommodate any type of "unit cell" collector model (here it is shown for spherical collectors) and arbitrary spatial variations of filter microstructure

including gradients in porosity/pore size as for example in the case of coated filters or multilayer structured filters (e.g. fibrous cartridges).

```
            ┌─────────────┐
            │    START     │
            └──────┬──────┘
            ╱ Read input file ╱
                   │
      ┌────────────────────────────┐
      │ Calculate u_w, μ, ρ of the gas │
      └────────────┬───────────────┘
         ┌──────────────────────┐
         │ Calculate d_co, b, w_s/x │
         └───────────┬──────────┘
      ┌────────────────────────────┐
      │        TEMPORAL LOOP        │
      │ Calculate k, w_soot, ΔP     │
      │  ┌──────────────────────┐   │
      │  │  PARTICLE SIZE LOOP   │   │
      │  │ SPATIAL EFFICIENCY LOOP │ │
      │  │ Calculate Pe, η_D, η_R, η_DR │ │
      │  │   Calculate E         │   │
      │  │ SPATIAL MICROSTRUCTURAL LOOP │ │
      │  │   Calculate d_c, ε    │   │
      │  │ Calculate E_num, E_vol │  │
      └────────────┬───────────────┘
              │ Print results │
            ┌──────────────┐
            │     STOP      │
            └──────────────┘
```
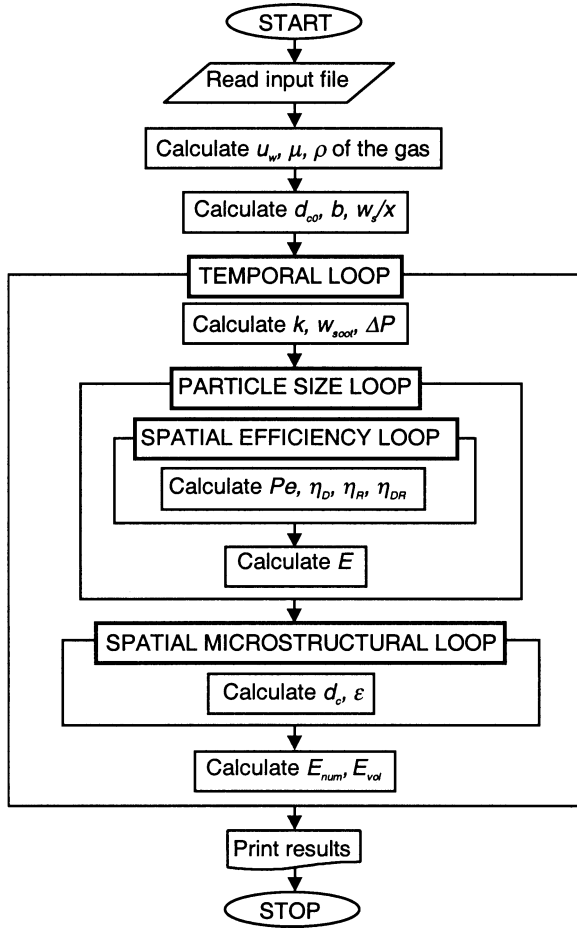
Figure 3. Flow chart of transient filter loading model. See Appendix III for details.

FILTRATION AND LOADING RESULTS – Eq. (1) is compared against three-dimensional (3-D) Computational Fluid Dynamics calculations in Figure 4. In addition, Eq. (1) is validated with experimental data [24] obtained fitting two types of filters in the exhaust of a single cylinder diesel engine, providing a 70 kg/hr flow at 280 °C and a 3.2 gr/hr particulate emission rate. Filter A had a filtration area of 2.1 m^2 and a cell opening of 1.44 mm (Figure 4), while filter B had a 1.53 m^2 filtration area and a cell opening of 2.11 mm (Figure 5). It is evident that there is excellent agreement between all three sets of data (analytical, numerical and experimental), establishing thus confidence in the use of Eq. (1) for filter pressure drop calculations at arbitrary loading.

A characteristic of the present filter pressure drop model is that it can accurately describe the non-linear behavior of the pressure drop trace for heavily loaded filters (particularly evident for filters with smaller cell openings, as in Figure 4).
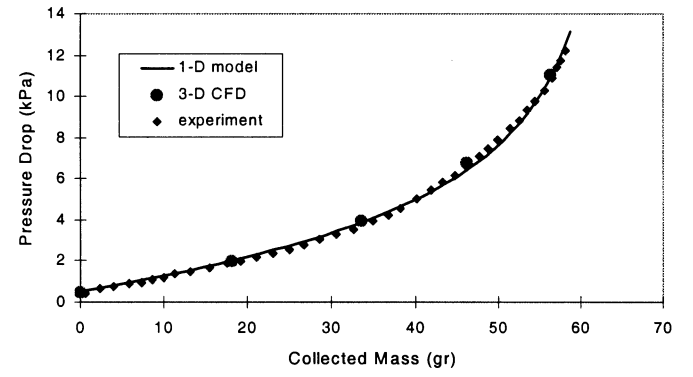

Figure 4. Experimental pressure drop curve for filter A [24], compared with analytical model, Eq. (1) and CFD results.
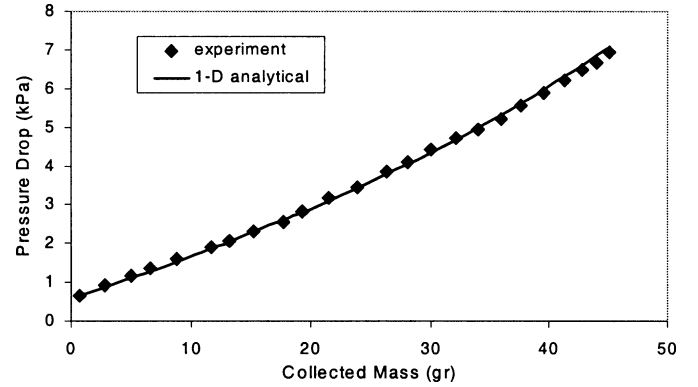

Figure 5. Experimental pressure drop curve for filter B [24], compared with analytical model, Eq. (1).

The particulate layer packing density $\rho_{soot,c}$ governs the non-linear behavior of the pressure drop, as the trap channel starts to be blocked, while the initial slope of the pressure drop rise curve depends mainly on the product of the particulate layer packing density and its Darcy permeability, k_{soot}. Pressure drop measurements of deliberately heavily loaded filters can be used in conjunction with the developed model to extract microstructural characteristics of the particulate layer grown in the filter. The present model provides thus for the first time a tool for the independent estimation of the particulate deposit packing density and permeability. For the particular examples shown in Figures 4 and 5 these characteristics are given in Table 6 and are very similar for the particulate layers grown on both filters.

Table 6. Particulate Microstructural Characteristics

Filter	Permeability (m^2)	packing density (kg/m^3)
A	3.2×10^{-14}	97
B	3.3×10^{-14}	110

It should be stated here that for accurate estimation of $\rho_{soot,c}$ it is necessary to have sufficient experimental data in the non-linear regime of pressure drop versus collected mass. Based on the analysis of such experiments a database of particulate layer characteristics (packing density and permeability) grown on many filter media under various operating conditions is developed at our laboratory to assist in rational filter selection and design.

Figure 6 depicts the simulation of the transient evolution of the size specific collection efficiency of a 10.5"x12" 100 cpi cordierite filter, exposed to the exhaust of a heavy duty diesel engine (0.236 Nm^3/s) at 260 $^\circ$C and a 18 gr/hr particulate mass emission rate. A typical diesel particle lognormal distribution was used as input to *FilSim*. It is evident that very quickly the "clean" filter collection efficiency increases to high values. The spatial distribution of collected particulate mass normalized with the total mass in the filter wall is shown in Figure 7. We observe an exponential distribution of the collected particulate mass along the filter wall thickness, that is expected to have significant implications in the case of catalyzed filters, where the local contact and particulate to catalyst ratio are important.
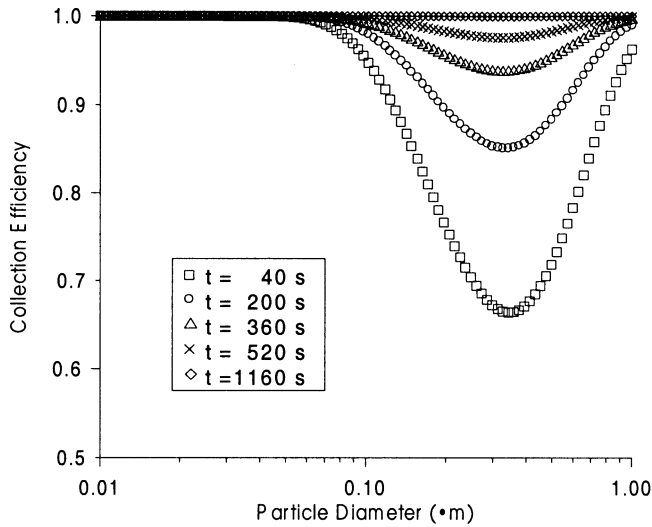

Figure 6. Simulation of the evolution of size specific collection efficiency of a cordierite filter.

Experimental validation of the filtration aspect of the model is provided in Figures 8 and 9 where the size distributions downstream of a corderite [25] and a sintered metal filter [26] are compared with model predictions. In the case of the sintered metal filter the comparison indicates that some post filter nuclei-mode particle formation [4,27] is taking place. Overall the filtration model is in good agreement with the data for the accumulation mode particles as was already found in [4] for another type of filter.
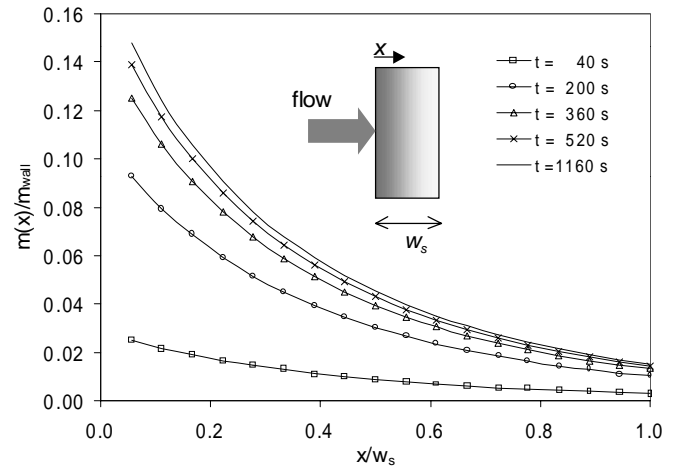

Figure 7. Simulation of the evolution of collected mass along the wall thickness of a cordierite filter.
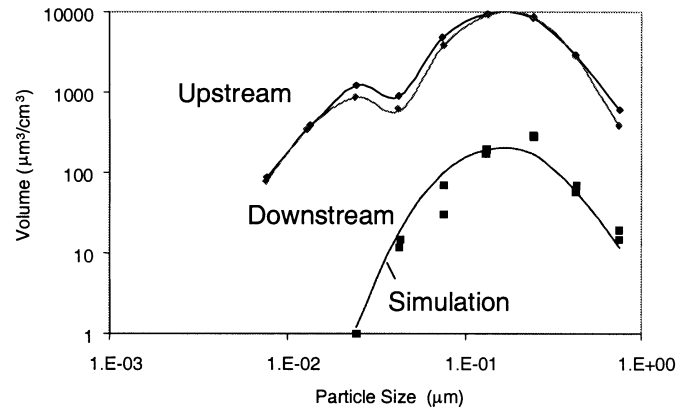

Figure 8. Particle size distributions measured upstream and downstream of a cordierite wall-flow filter [25], together with theoretical prediction.
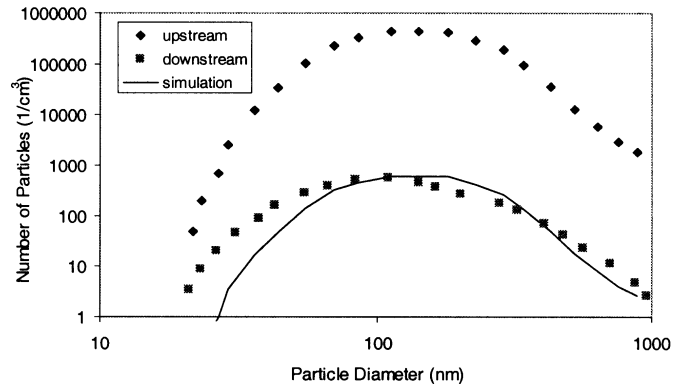

Figure 9. Particle size distributions measured upstream and downstream of a sintered metal filter [25], together with theoretical prediction.

The transient filtration model is used to simulate the experimental data in [22] on the pressure drop of various cordierite filter types (Figure 15 in [22]). The filters were

6

exposed to the exhaust of a heavy duty diesel engine at 0.236 Nm^3/s and 260 °C. A particulate mass flow of 18 gr/hr as given in the paper was used for the simulation. Since it was referred to as "soot" in the paper [22] we assumed that it corresponded to the emission rate of the solid particulate that would be actually entering the filter. All DPF's had dimensions of 10.5"X12.0", cell density of 100 cpi and a wall thickness of 0.017 in. The reader is referred to the original paper [22] for additional experimental details. The simulation of these data was performed with the parameter values shown in Table 7. All parameters except the last three in Table 7 were fixed to the indicated values. The first two parameters in Table 7 are nominal values from the filter manufacturer, the clean filter permeability was estimated from the first experimental data point of Figures 10-13, and the cake packing density value was estimated based on our experience with heavily loaded filters (see also Table 5). A non-linear regression code using the Levenberg-Marquardt method [28] was written to estimate the values of the last three parameters in Table 7 from the experimental data.

Table 7. Particulate Microstructural Characteristics

FILTER:	EX-47	EX-54	EX-66	EX-80
d_{pore} (μm)	13.4	24.4	34.1	12.5
ε (%)	48	50	50	48
k_0 (m^2)	2.4×10^{-13}	3.3×10^{-13}	3.5×10^{-13}	1.8×10^{-13}
$\rho_{soot, c}$	91	91	91	91
k_{soot} (m^2)	1.8×10^{-14}	1.9×10^{-14}	2.1×10^{-14}	2.2×10^{-14}
$\rho_{soot, w}$	14.10	12.24	12.22	8.26
ψ	0.9203	0.9246	0.9201	0.8651

Figure 10. Comparison of transient filtration model pressure drop prediction against experiments [22] for a Corning EX-47 filter.

Figure 11. Comparison of transient filtration model pressure drop prediction against experiments [22] for a Corning EX-54 filter.
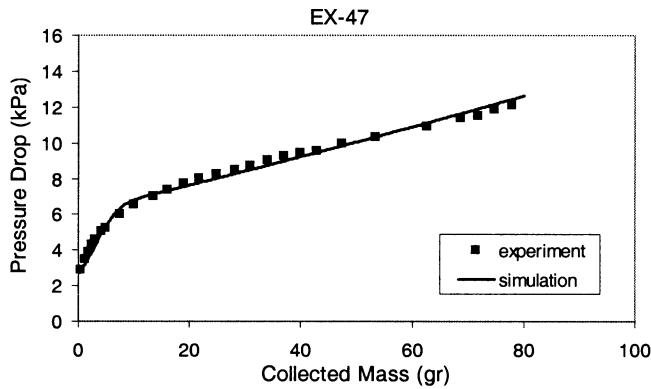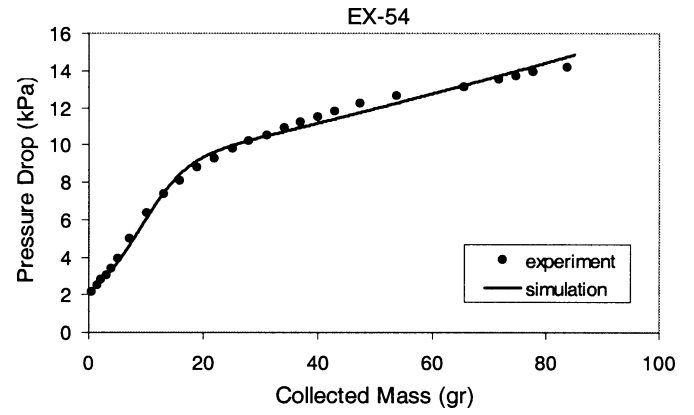

Figure 12. Comparison of transient filtration model pressure drop prediction against experiments [22] for a Corning EX-66 filter.

Figure 13. Comparison of transient filtration model pressure drop prediction against experiments [22] for a Corning EX-80 filter.
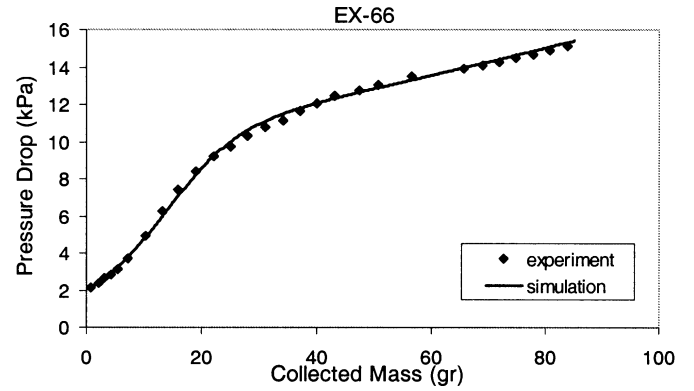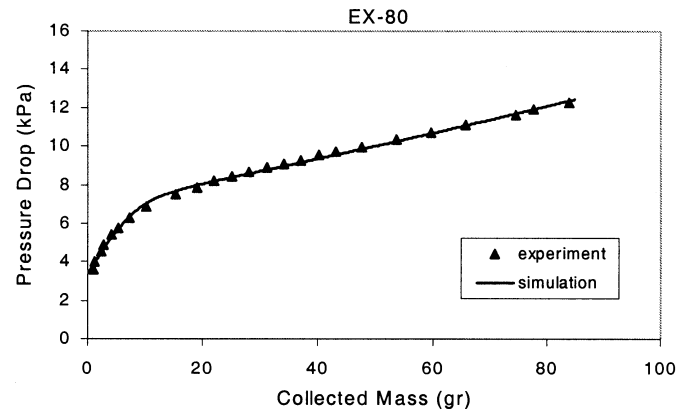
Examining Figures 10-13, we observe that the developed transient filtration model describes very well the entire transition from deep bed-to-cake behavior for all tested

filters. In addition the estimated parameters of all particulate layers (Table 7) are in close agreement with each other, establishing thus the internal consistency of the model. It is interesting to notice the low packing density determined for the particulate collected inside the filter wall vs. that of the particulate cake. This is consistent with the notion of *percolation*, where small "islands" of particulate dispersed into the (deep-bed like) filter wall, can cause substantial increase of pressure drop by pore bridging/blocking.

REGENERATION BEHAVIOR

THEORETICAL FRAMEWORK – There are a lot of aspects that must be included in a comprehensive model for the regeneration behavior of a particulate filter. In general, there are three coexisting scales ("levels") which the modeller of particulate traps must take into account. The first level refers to the phenomena occurring across the particulate layer and the porous filter walls, the second level to the phenomena occurring along the filter channels and the third level refers to the phenomena at the macroscopic scale of the trap. Submodels at each level must be developed and properly combined in order to derive a model of the entire process. In the following, these three levels are discussed in more detail.

Level I. Filter wall scale – The exhaust stream can be assumed to be always in a quasi-steady state, since the residence time of the exhaust gas as it transverses the filter wall, is very small compared to the characteristic scale of variations of the filter inlet conditions (velocity, temperature, oxygen content). The fluid mechanics at this level is trivial (just a constant filtration velocity). A separate differential mass balance must be written for each active species (all species which take part in a reaction in the particulate layer, e.g. O_2, NO_2, gaseous and adsorbed hydrocarbons). In addition, a transient energy balance equation must be derived for the temperature distribution across the particulate layer and porous wall.
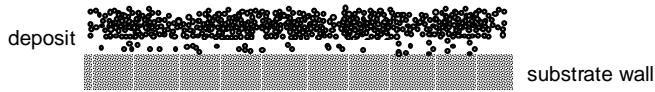

deposit

substrate wall

Figure 14. Schematic of filter wall.

A complication arises from the oxidation of the particles trapped in the pores and on the wall surface, that necessitates the solution of a moving boundary problem. Bissett addressed the above problem [29, 30] and showed using a singular perturbation expansion valid for small thermal Peclet numbers (a very good assumption) that the temperature can be assumed uniform across the particle layer and porous wall. This leads to a great simplification, since only the species mass balances must be integrated across the particle layer and filter

thickness. This integration can be done analytically for some simple cases (e.g. for the case of O_2 or O_2/NO_2 particulate oxidation), while in more complex cases the integration has to be performed numerically. Application of the methodology to a case simulating our experiments with catalytic coatings and coupled reactions among the active species (described later) is given in Appendix IV.

Structural considerations for the particulate deposit and the porous filter wall (possibly serving as a substrate for a catalytic coating) must also be taken into account in Level I (Figure 14). Recently, Konstandopoulos and Kostoglou developed [31] and applied [14, 32] a mesoscopic microstructural filter model (the so-called two-layer model) to describe the effect of the catalytic coating of the porous walls, supplemented with a general "mixture-model" for the carbonaceous particulate-catalyst promoted oxidation kinetics, taking explicitly into account the particulate-catalyst contact. Appendix IV describes the extension of that model to account for the presence of NO_2 in the filter inlet, to investigate NO_2-regenerative technologies (currently practiced with uncatalyzed filters) in combination with catalyzed filters. Such combinations could lower the dependence of NO_2-regenerative technologies to high engine-out NO_x concentrations, as NO_x emission standards become tighter.

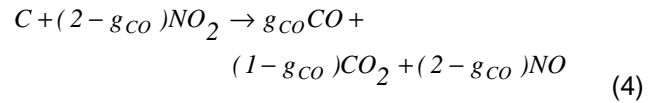The relevant reactions that are assumed to describe the process are:

Thermal particulate oxidation

$$C + (1 - f_{CO}^{the}/2)O_2 \rightarrow f_{CO}^{the}CO + (1 - f_{CO}^{the})CO_2 \tag{2}$$

Catalytic particulate oxidation

$$C + (1 - f_{CO}^{cat}/2)O_2 \rightarrow f_{CO}^{cat}CO + (1 - f_{CO}^{cat})CO_2 \tag{3}$$

NO_2-assisted particulate oxidation

$$C + (2 - g_{CO})NO_2 \rightarrow g_{CO}CO + (1 - g_{CO})CO_2 + (2 - g_{CO})NO \tag{4}$$

NO to NO_2 catalytic oxidation

$$2NO + O_2 \rightarrow 2NO_2 \tag{5}$$

Where the selectivities f_{CO}^i, g_{CO} (*i = the* or *cat*) of the reactions are given explicitly in Appendix IV.

In the general case the model of Level I serves to provide a "constitutive relation" for the local reaction rate to the Level II model.

Level II. Filter channel scale – If the transient behavior of the filter is slow with respect to the residence time of the exhaust gas as it travels across the filter, then the quasi-steady state approximation for the exhaust flow in the channels can be used.
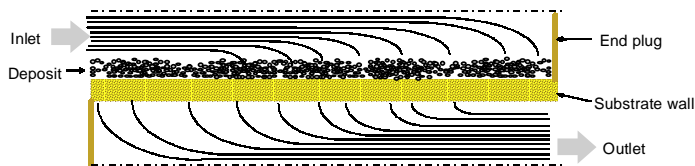
Figure 15. Schematic of filter channel.

A rigorous approach for this scale was first provided by Bissett [33]. His one-dimensional model includes the mass and momentum balances for a representative inlet and outlet channel (Figure 15) plus a Forcheimer modified Darcy's law for the porous filter wall. As discussed in the previous section on the loading behavior, this approach for the fluid mechanics has been validated against 3-D CFD and experiments, see also [4,17,19]. The reduction in dimensionality of the problem possible with this approach, in connection with its proven accuracy, support its choice as the best available, for a fluid mechanical submodel for the trap channels.

To model the particulate oxidation process, additional equations must be solved coupled with the fluid mechanical submodel. These include: quasi-steady state energy balances for the exhaust gas stream in the inlet and outlet channel, transient energy balance for the system porous wall-particulate layer and an evolution equation for the particulate layer mass (or thickness). If the inlet conditions to the trap can be assumed to be spatially (radially) uniform, solving the model for two representative channels (inlet and outlet) is equivalent to solving it for the entire trap (assumed radially homogeneous). This approach was successfully validated against experimental results in [14, 32]. In the general case the Level II model serves to provide the laws of phase interactions for the model of Level III.

Level III. Trap scale – This is the macroscopic scale of the DPF. The need for a model at this scale arises from the possible existence of inlet radial non-uniformities. Radial variations of the exhaust gas stream velocity and temperature at the inlet of the filter have been assessed by simulating the exhaust system with CFD (see [17]). Some previous attempts for modeling at this level are based on the approximation of the radial non-uniformities through a number of "zones" (collections of several channels) along the radius of the filter with thermal coupling between adjacent "zones" [34]. This approach requires closure for the "zone" interactions.

A self-consistent continuum model for the entire porous filter, is currently under development at our laboratory following the principles of volume averaging in multiphase flows [35]. The three phases in the trap are the exhaust gas in the inlet channels, the exhaust gas in the outlet channels and the solid phase, whereas diesel particulate is modeled as a species component distributed in all three phases. The advantage of the multiphase continuum formalism is that all relevant phenomena can be described by a compact set of Partial Differential Equations, easily integrated into the framework of CFD

codes (in-house or commercial). Figures 16-18 depict 3-D flow simulation of several types of diesel particulate filters (wall-flow honeycomb, foam and fibrous cartdridge filters) at the macroscopic scale
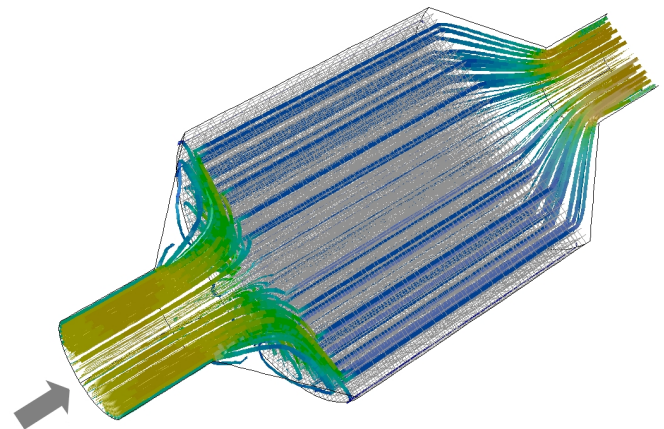
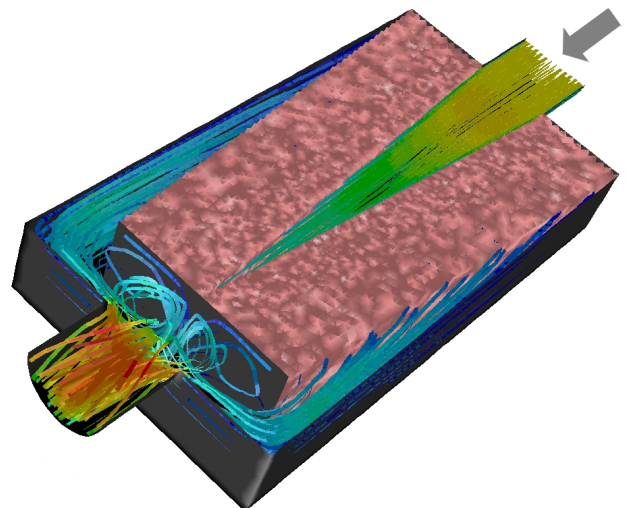

Figure 16. Flow simulation of honeycomb DPF.

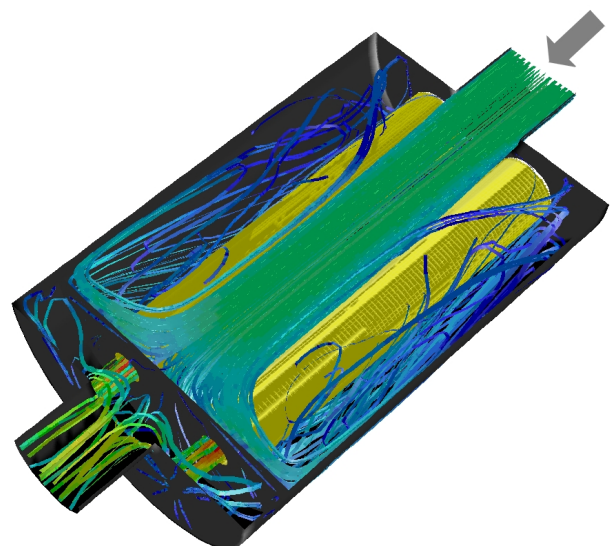Figure 17. Flow simulation of V-shaped foam DPF.

Figure 18. Flow simulation of fibrous cartridge DPF.

9

NO$_2$-ASSISTED PARTICULATE OXIDATION

Experimental – NO$_2$ oxidation of diesel particulate was studied on prototype catalyzed ceramic filter disks (of diameter 60 mm and thickness about 1 mm) loaded in a special pilot scale filter testing unit (Figure 19), at the Aerosol & Particle Technology Laboratory of FORTH/ CPERI [36]. The filters were exposed to a constant exhaust flow from a passenger car turbo-charged direct injection diesel engine with a 1.9 Lit displacement (rated at 66 kW/4000 rpm) operated at 2400 rpm and 50% load, coupled to a hydraulic bolt-on dynamometer.

The filter disk is held in place sandwiched between two gaskets cut from heat expanding fibrous mat in a stainless-steel holder, housed in a heated stainless-steel reactor. The exposed filter diameter to the flow is 40 mm. As shown in the diagram of Figure 19, the unit is instrumented with thermocouples and incorporates a by-pass valve that permits isolation of the filter from the exhaust flow under an inert (N$_2$) atmosphere. A heated tube before the reactor heats the exhaust gases to the desired temperature. The unit sits on a bench that incorporates sampling pumps and ancillary controllers and transducers to maintain constant volume flow through the filter. A dedicated data acquisition computer collects temperature, pressure and exhaust gas analysis data from the unit.

To study the NO$_2$-particulate reaction on the catalyzed filters, the filters were first loaded with particulate from the engine exhaust. Subsequently they were in-situ exposed under a temperature ramp (3 °C/min), in the range of 300 °C to 500 °C, to a synthetic exhaust flow of 3 NLit/min. In these conditions the presence of the catalyst can promote the re-oxidation of NO (resulting from NO$_2$ reduction by the particulate) back into NO$_2$ and accelerate thus the rate of particulate oxidation.

Results – Particulate oxidation was followed by monitoring the concentration of CO$_2$, NO and NO$_2$ behind the filter as well as the pressure drop evolution across the filter. To clarify the influence of NO$_2$ three types of experiments were performed.

- Oxidation by a 10% O$_2$ in N$_2$ stream (Figure 20)
- Oxidation by a 400 ppm NO$_2$ in N$_2$ stream (Figure 21)
- Oxidation by a 400 ppm NO$_2$/10% O$_2$ in N$_2$ stream (Figure 22)
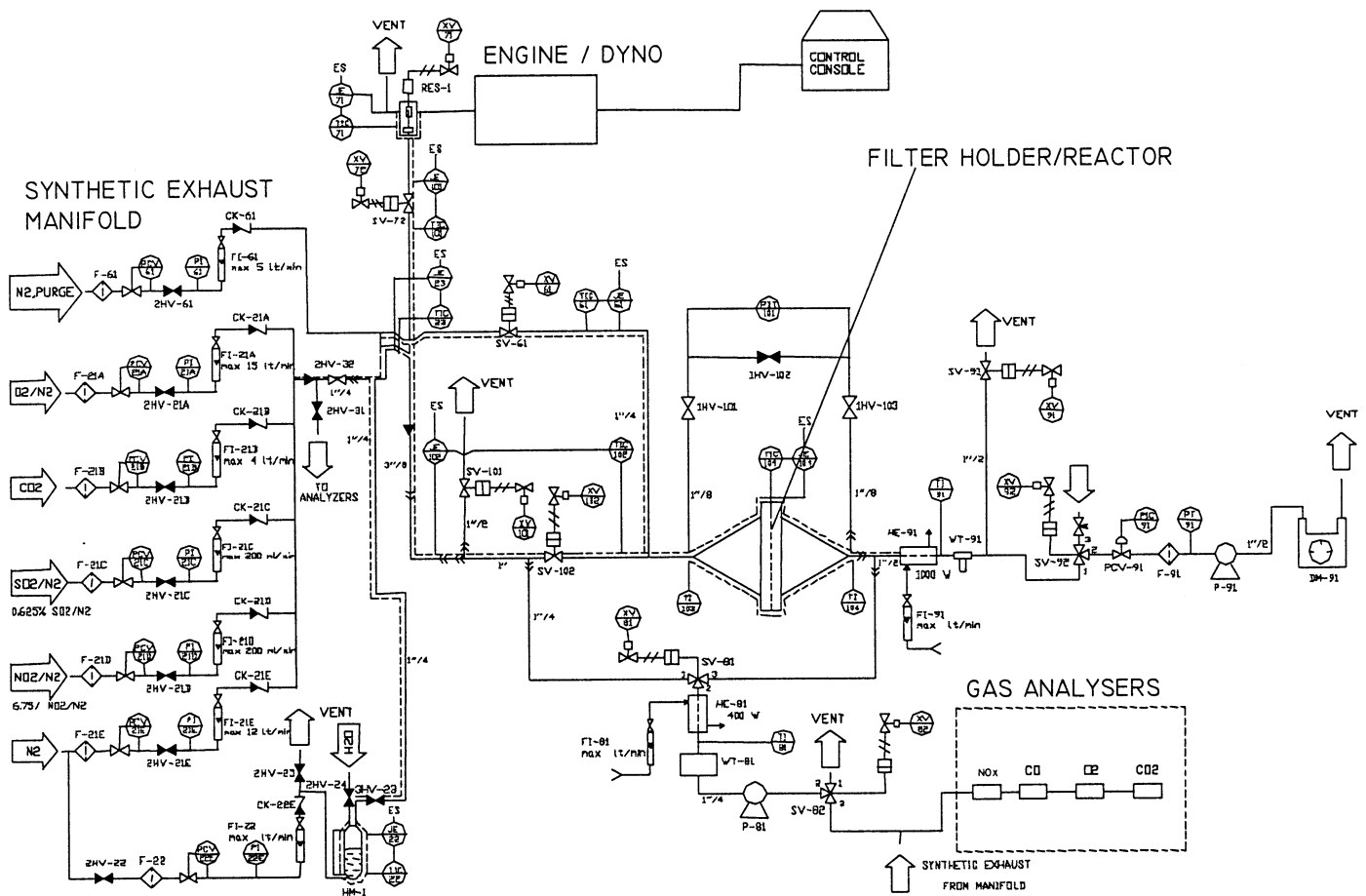

Figure 19. Flow chart of the experimental set-up used for loading prototype particulate filters from diesel exhaust and studying their regeneration under controlled conditions of feed composition and temperature.

The dotted lines in Figures 20-22 are based on the application of the NO_2 assisted particulate oxidation model described in Appendix IV. The NO_2-particulate oxidation kinetics were adjusted to fit the NO_2 evolution profile and then the CO_2 profile was computed without any other adjustment to assess the validity of the assumed reaction mechanism. A high degree of consistency is observed between model and experiments building confidence in the use of the model to extract kinetic data from these and similar experiments. The activation energies of reactions (Eqs. 2, 4, 5) extracted from these experiments are shown in Table 8. The data imply that the catalytic coating has minimal effect on the direct catalytic oxidation of the particulate, however its presence makes possible the acceleration of the particulate oxidation rate through the oxidation of NO to NO_2 which in turn oxidizes the particulate. This is evident comparing Figure 21 to Figure 22. It is seen in Figure 22 that in the presence of O_2, there is significantly higher amount of NO_2 remaining due to the action of the catalytic coating towards NO_2 production. On the contrary, in Figure 21 NO_2 is almost consumed entirely when the particulate oxidation reaches its highest rate.

Table 8. Activation Energies of Eqs. (2), (4) and (5) on Catalyzed Filter

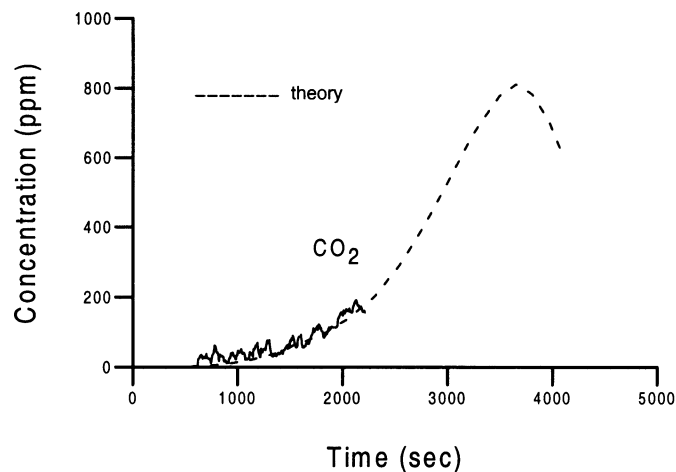| Reaction	E/R in K
$C + O_2$	18040.
$C + NO_2$	14650.
$NO + \frac{1}{2} O_2$	10900.

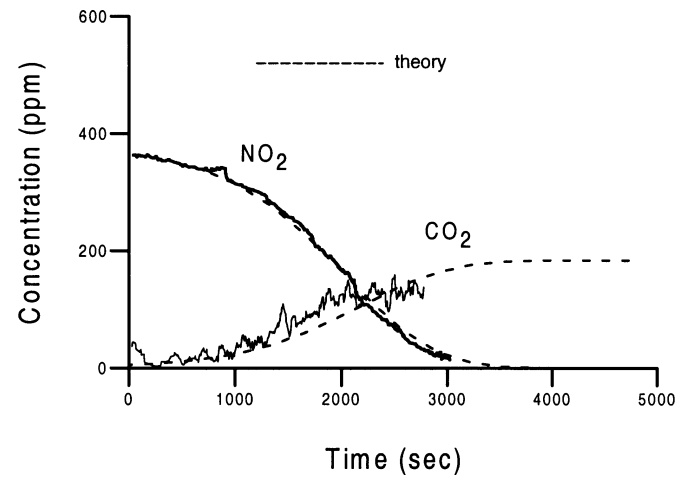Figure 20. O_2-particulate reaction on catalyzed filter.

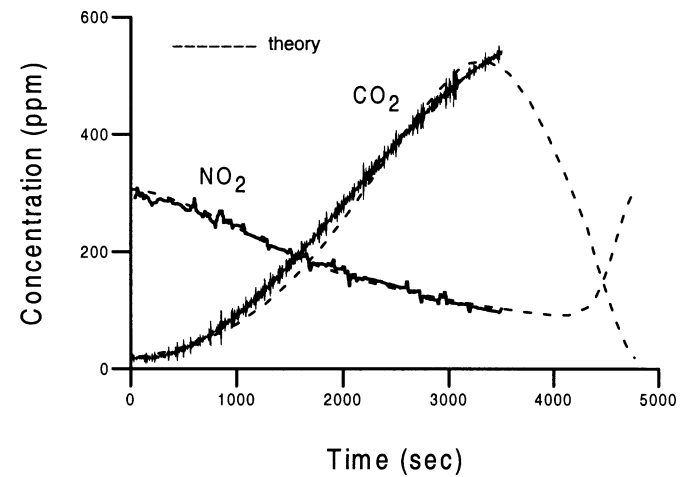Figure 21. NO_2-particulate reaction on catalyzed filter in the absence of O_2.

Figure 22. NO_2-particulate reaction on catalyzed filter in the presence of O_2.

AGING OF FILTER PRESSURE DROP DUE TO ASH

A critical factor that affects the expected lifetime of DPF's is ash accumulation after repeated regenerations. The origin of the ash is the lubricating oil additives, engine wear as well as the fuel, especially if it contains additives for regeneration promotion. The problem of filter plugging by ash accumulation is stated as one of the most important problems by many diesel engine manufacturers [37]. It is therefore interesting to develop and validate appropriate models for the aging behavior of the filter pressure drop, to assist the life cycle analysis and optimization of DPF's for a particular application. The transient filter loading model developed in this paper is indispensable in this respect, since it can describe not only the collection of diesel particulate but also the accumulation of ash particles inside the filter, provided that appropriate ash deposit microstructural properties are employed.

Figure 23 depicts the application of the developed pressure drop model to the experimental data of [38] in order to estimate ash layer microstructural properties.
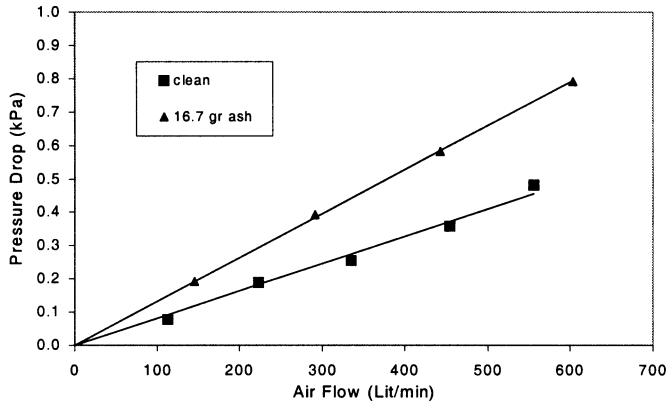

Figure 23. Experimental points of pressure drop for a 100 cpi cordierite 2.66"x12" filter [38] compared with theory (continuous lines) for the clean filter [4] and after accumulation of 16.7 gr of ash [present model based on Eq. (1)].

Based on first principles, one would expect the ash packing density to be of $O(10^3)$ kg/m^3, while its permeability for μm-sized particles to be of $O(10^{-14})$ m^2. Ash packing density was estimated by an independent experiment where ash collected from a regenerated trap, was poured into a graduated tube and its volume and mass were measured at various stages of compaction. This resulted in an ash packing density between 400 and 1000 kg/m^3. The loading model for these values of packing density then estimates ash layer permeability between 2.77 and 7.4 x 10^{-14} m^2. Applying the Kuwabara model for the permeability [4, 21, 39] one can estimate that these permeabilities are consistent with an "effective" ash particle size between 0.5 and 2 μm. Measurements of ash particle size distribution were conducted with two techniques available at the APT Laboratory: an aerodynamic time-of-flight individual particle count, technique with a minimum detection limit of 0.2 μm (TSI Aerosizer) and a laser ensemble diffraction technique (Malvern Mastersizer). Figure 24 shows the ensemble diffraction based ash particle size distribution, while Figure 25 shows the time-of-flight measured size distribution (by number, area and volume). Considering that the optical technique measures some large agglomerates (peak around 100 μm in Figure 24) which are broken down by the dispersion in the hypersonic flow field of the Aerosizer, we conclude that both techniques indicate a substantial amount of ash particle volume to lie between 1 and 10 μm.

Ash particles were also observed in the Scanning Electron Microscope (Figure 26). It can be seen that ash particles are aggregates (mainly in the 1-10 μm range) of smaller units. The smaller units have characteristic dimensions that broadly agree with the permeability-based estimates of "ash effective size".
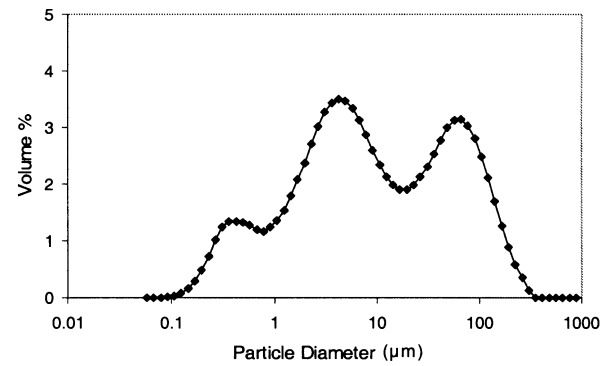

Figure 24. Size distribution of ash measured with the Mastersizer.
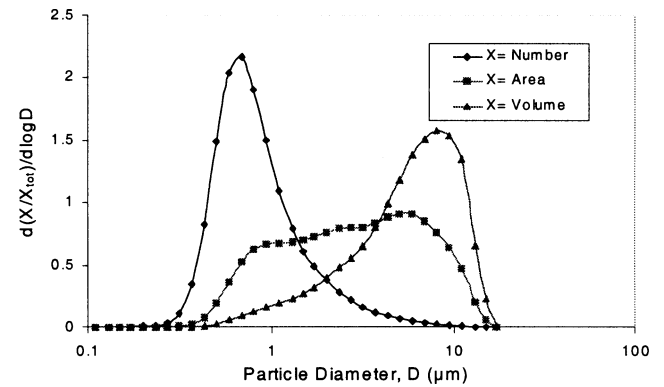

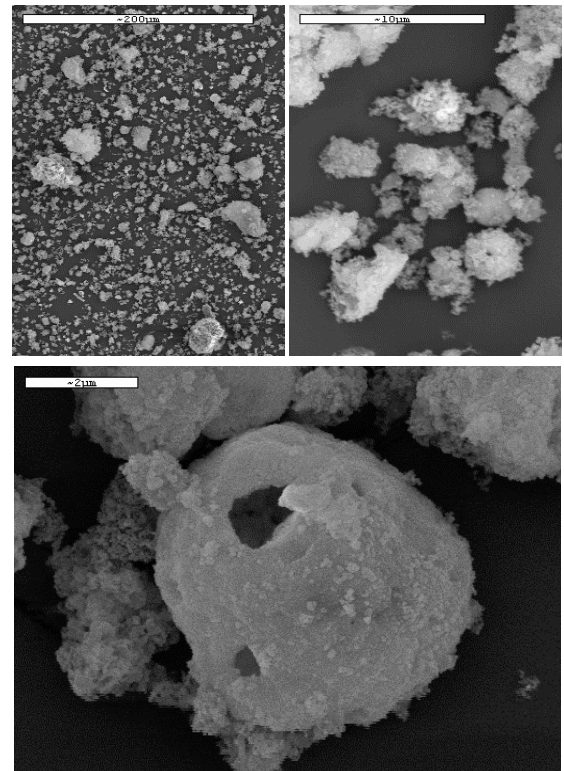Figure 25. Size distribution of ash measured with the Aerosizer.

Figure 26. SEM pictures of ash at different magnifications.

In the case of fuel-borne catalysts, the size distribution of the resulting ash most likely depends on the catalyst dose. Burtcher et al. [40] presented interesting experimental data on this phenomenon (Figure 27), for a Cerium fuel-borne catalyst. In that study, a locus of catalyst dosage is seen to exist below which the Cerium is scavenged by the soot particles, and above which Cerium nucleates homogeneously into (oxide) nano-particles giving rise to a distinct mode in the size distribution [40, 41].
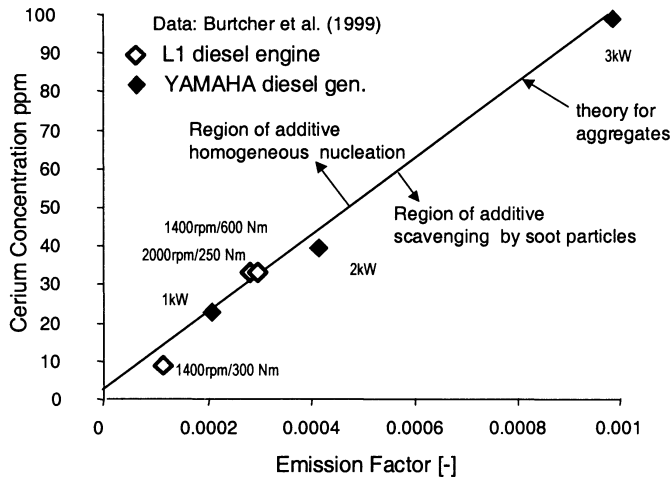
Figure 27. Cerium fuel-borne catalyst homogeneous nucleation locus. Experiments [40, 41] and theory [42].

Assuming that the scavenging rate is proportional to the available particulate area it can be shown [42] that for soot aggregates the points on Figure 27 should fall on a straight line. As seen in Figure 27 this is well supported by the experiments. We expect the activity of the fuel-borne catalyst to become less above the line in Figure 27, as it will exist in the form of individual particles that would exhibit poorer contact with the diesel particulate than the catalyst scavenged directly and incorporated inside the particulate. We anticipate thus that any dose above the locus in Figure 27 would contribute more into the ash aging of the filter, rather than to the improvement of its regeneration and therefore it should be avoided, to prevent fast aging of the filter pressure drop. Konstandopoulos and Kostoglou [32] have found analyzing the data of Tan et al. [43] for a Copper fuel-borne catalyst, that a dosage of 33 ppm was already in contact with 95% of the available soot surface area and therefore increasing the dose to 66 ppm would induce no further enhancement, a fact supported by the experiments of [43].

Combining the available information on ash properties a simulation of ash accumulation into 9"x12" cordierite filters of 100 and 200 cpi exposed to the exhaust of a diesel engine at 0.33 actual m^3/sec and 310 °C was performed for two values of ash emission rates, namely 7 and 14 gr/1000km.
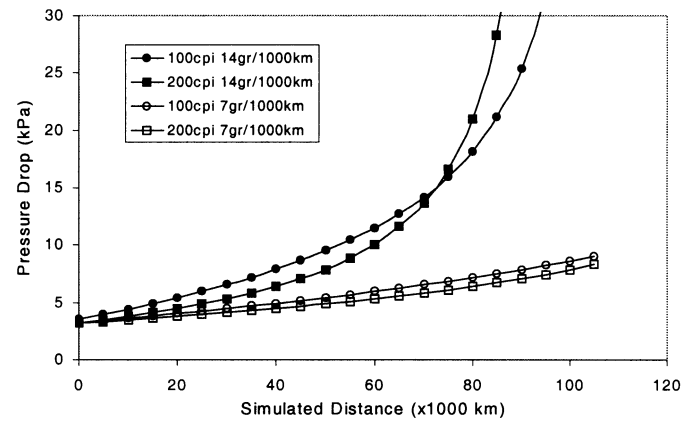
Figure 28. Pressure drop aging simulation of a 9"x12" cordierite wall-flow filter.

It is interesting to note in Figure 28 for the higher ash emission simulations, that after about 75000 km the 200 cpi filter loses its better aging behavior (lower pressure drop rise due to ash accumulation) over the 100 cpi filter, as both filters start to become severely plugged with ash. The results shown in Figure 28 illustrate the utility of the aging model for performing Life Cycle Analysis as well as in supporting the selection process of diesel particulate filters.

CONCLUSIONS

Optimized diesel particulate emission control system design encompasses selection of porous media, filter geometric configuration and regeneration strategies. The process can be significantly aided through the use of validated mathematical models based on rigorous theoretical descriptions of the fundamental underlying physicochemical processes. In the present paper we have outlined the development of state-of-the-art, experimentally validated analytical and numerical models for three critical aspects of the operation of diesel particulate emission control systems, namely transient filter loading, catalyzed/NO_2-assisted filter regeneration and filter pressure drop aging due to ash accumulation. The major findings in each of these areas are stated below:

TRANSIENT FILTER LOADING

1. By extending the clean filter pressure drop model of [17], an analytical expression has been derived Eq. (1), for the pressure drop of arbitrarily loaded filters that operate in the cake filtration regime. The expression was shown to be in excellent agreement with "presumably exact" 3-D CFD simulations and with experimental data collected with honeycomb filters fitted in the exhaust of a diesel engine. The simplicity of the model makes it a valuable tool for optimized preliminary diesel particulate filter selection and design.

2. To describe the initial deep-bed filtration regime of some filters a transient filtration simulator was developed (*FilSim* v. 1.0) applying the notion of "unit cell" filtration theory, locally across the filter wall. The simulator predicts the transient collection efficiency and pressure drop of diesel particulate honeycomb filters with arbitrary wall structure and was shown to describe with excellent accuracy transient loading experiments, available in the literature for a variety of filter grades. The validated simulator can be used for designing tailored filter structures for particular applications, e.g. for catalyzed filter substrates with optimized diesel particle-catalyst contact (currently in progress).

FILTER REGENERATION

1. The regeneration process of prototype small scale catalyzed filter disks, loaded in-situ from the exhaust of a diesel engine was experimentally studied in the presence of NO_2 in a specially constructed testing unit. The results indicate the potential benefits that catalyzed filters can bring to NO_2-regenerative technologies, through the in-situ re-oxidation of NO (produced by the carbon-NO_2 reaction) back to NO_2 alleviating the dependence on high engine-out NO_X concentrations.

2. A previously published regeneration model by the authors [14, 31, 32] was extended to account for the presence of NO_2 on particulate oxidation and was shown to describe very well the collected experimental data. The model is very useful for the design of next-generation NO_2-regenerative technologies employing catalyzed filters.

FILTER PRESSURE DROP AGING DUE TO ASH ACCUMULATION – The transient filtration model was adapted to describe the process of ash accumulation after repeated regenerations of the filter. Using filter pressure drop aging data from the literature and simple characterizations of ash particles collected from regenerated filters, a validated filter pressure drop aging model was developed. The aging model can be used for performing filter Life Cycle Analysis as well as in supporting the sizing process of diesel particulate filters for applications where extended life time is required (e.g. in heavy-duty trucks).

The integration of the derived models into the practice of engine/vehicle manufacturers and their suppliers (currently in progress) will lead to a systematic and hence more efficient, concurrent engineering procedure for optimized design of emission reduction components and their interface into complete systems.

REFERENCES

1. **Diesel Exhaust Aftertreatment**, SAE Special Publication, SP-1414, 1999

2. **Diesel Exhaust Aftertreatment**, SAE Special Publication, SP-1313, 1998.

3. **Diesel Exhaust Aftertreatment**, SAE Special Publication, SP-1227, 1997.

4. Konstandopoulos, A. G., Johnson, J. H., "Wall-flow diesel particulate filters-their pressure drop and collection efficiency" *SAE Trans.* **98** sec. 3 (*J. Engines*) *Paper No. 890405*, p. 625, 1989.

5. http://www.dieselnet.com

6. Howitt, J., Montierth, M., "Cellular ceramic diesel particulate filter", *SAE Paper No. 81104*, 1981.

7. Roth, P., Eckhardt, T., Franz, B., Patschull, J. "H_2O_2-assisted regeneration of diesel particulate traps at typical exhaust gas temperatures" *Combust. Flame* **115**, p. 28, 1998.

8. Lueders, H., Stommel, P., Geckler, S. "Diesel exhaust treatment-new approaches to ultra low emission diesel vehicles", *SAE Paper No. 1999-01-0108*, 1999.

9. Christensen, H., Dinesen, J., Engell, H., Hansen, K., "Electrochemical reactor for exhaust gas purification" *SAE Paper No 1999-01-0472*, 1999.

10. Hawker, P., Myers, N., Huthwohl, G., Vogel, H., Bates, B., Magnusson, L., Bronneberg, P., "Experience with a new particulate trap technology in Europe" *SAE Paper No 970182*, 1997.

11. Neeft, J., **Catalytic oxidation of soot; Potential for the reduction of diesel particulate emissions**, Ph.D. Thesis, Tech. Univ. Delft, 1995.

12. Jelles, S., Makkee, M. Moulijn, J., Acres, G., Peter-Hoblyn, J., "Diesel particulate control. Application of

an activated particulate trap in combination with fuel additives at an ultra low dose rate", *SAE Paper No 1999-01-0113*, 1999.

13. http://www.dieselnet.com/news/9904peugeot.html

14. Konstandopoulos, A., Kostoglou, M., "Periodically reversed flow regeneration of diesel particulate traps" *SAE Paper No 1999-01-0469*, 1999.

15. Page D. L., MacDonald J. R., Edgar B. L., "The QuadCAT^{TM} Four-Way Catalytic Converter: An Integrated Aftertreatment System for Diesel Engines", *SAE Paper No 1999-01-2924*, 1999.

16. Oh, S., McDonald, J., Vaneman, G., Hegedus, L., "Mathematical modeling of fibrous filters for diesel particulate-Theory and experiments", *SAE Paper No 810113*, 1981.

17. Konstandopoulos, A., Skaperdas, E., Warren, J., Allansson, R., "Optimized filter design and selection criteria for continuously regenerating diesel particulate traps", *SAE Paper No 1999-01-0468*, 1999.

18. *Auto Emissions Magazine*, Corning Inc., No. 14, 1999.

19. Masoudi, M., Zinc, U., Then, P. M., Cash, T., Thompson, D., Heibel, A., "Predicting pressure drop of diesel particulate filters: modeling and experiment", *SAE Paper No 2000-01-0184*, 2000.

20. Kwetkus, B. A., Egli, W. "The ceramic monolithic filter module: filtration properties and DeNox potential", in **High Temperature Gas Cleaning** (Eds. Schmidt et al.), p.278, Institut fuer Mechanische Verfahrenstechnik und Mechanik, Karlsruhe, 1996.

21. Tien C., **Granular Filtration of Aerosols and Hydrosols**, Butterworths, New York, (1989)

22. Murtagh, M. J., Sherwood, D. L., Socha, L. S. Jr. "Development of diesel particulate filter composition and its effect on thermal durability and filtration performance", *SAE Paper No 940235*, 1994.

23. Suresh, A., Khan, A., Johnson, J. H. "Pressure Drop and Permeability of Clean and Particulate Loaded Filters", *SAE Paper No 2000-01-0476*, 2000.

24. Final Report to the European Commission on BRITE–EURAM III Project No. 1531-BE95-1984, March 1999.

25. Harvey, G. D., Baumgard, K. J. Johnson, J. H. Gratz, L. D., Bagley, S. T., Leddy, D. G. "Effects of a Ceramic Particle trap and Copper Fuel Additive on Heavy-Duty Diesel Emissions", *SAE Paper No 942068*,1994.

26. Rogers, T., "Solving Ultrafine Particulate Emissions", *Engine Technology International* '98 Annual Review p. 17, 1998.

27. Abdul-Khalek, I. S., Kittelson, D. B., Graskow, B. R., Wei Q., Brear F. "Diesel Exhaust Particle Size: Measurement Issues and Trends", *SAE Paper No 980525*, 1998.

28. Press, W.H., Teukolsky, S.A., Vetterling, W.T. and Flannery, B.P., **Numerical Recipes. The art of scientific computing**, Second Edition, Cambridge University Press, Cambridge, 1992.

29. Bissett, E., "Thermal regeneration of particle filters with large conduction" *Math. Model.* **8**, p.1, 1985.

30. Bissett, E., Shadman, F., "Thermal regeneration of diesel particulate monolithic filters" *AIChE J.* **31**, p.753, 1985.

31. Konstandopoulos, A., Kostoglou, M., "A mathematical model of soot oxidation on catalytically coated ceramic filters" *Advances in Vehicle Control and Safety*, Amiens, France, p.137, 1998.

32. Konstandopoulos, A.G., Kostoglou, M. "Reciprocating flow regeneration of soot filters", *Comb. and Flame*, in press, 2000.

33. Bissett, E., "Mathematical model of the thermal regeneration of a wall-flow monolith diesel particulate filter" *Chem. Eng. Sci.* **39**, p.1232, 1984.

34. Aoki, H., Asano, A., Kurazono, K., Kobashi, K., Sami, H., "Numerical simulation model for the regeneration process of a wall-flow monolith particulate filter", *SAE Paper No 930364*, 1993.

35. Kuo, K. **Principles of combustion**, John Wiley & Sons, New York, 1986.

36. Papaioannou, E., Zarvalis, D., Konstandopoulos A. G, "Influence of NO_2 on soot particles oxidation" *Proc. Second Panhellenic Symposium of Chemical Engineers*, p. 325, 1999.

37. Minutes of European Commission *PREMTECH Network Workshop on Aftertreatment*, Oct. 14-15, 1999, FORTH/CPERI, Thessaloniki.

38. Sachdev R., Wong V. and Shahed S., "Effect of ash accumulation of diesel exhaust particulate traps" (SAE 830182)

39. Lee K. W., Gieseke J. A., "Collection of aerosol particles by packed beds", *Env. Sci. Tech.* **13** (4), p.1761, 1978.

40. Burtscher H, Matter U., Skillas G.,"The effect of fuel additives on diesel engine particulate emissions" *J. Aerosol Sci.*, **30**, p. S851, 1999

41. Burtscher H, Skillas G., Baltensperger, U., Matter U.,"Particle Formation due to Fuel Additives" *Proc. 3rd Int. ETH Workshop on Nanoparticle Measurement*, August 9-10, Zurich, 1999.

42. Konstandopoulos, A.G., Kostoglou, M. "A Population Balance Study of the Simultaneous Evolution of Soot and Fuel Additive-Originating Particles", in preparation, 2000.

43. Tan, J., Opris, C., Baumgard, K., Johnson, J. H. "A study of the regeneration process in diesel particulate traps using a Copper fuel additive", *SAE Paper No 960136*, 1996.

44. *VDI-Waermeatlas*, 6. Aufl., VDI-Verlag Duesseldorf, 1992

45. Fluent Inc., **Fluent 5 User's Guide**, July 1998.

46. Friedlander S. K., **Smoke, dust and haze: Fundamentals of aerosol behavior**, John Wiley & Sons, New York, 1977.

47. Konstandopoulos, A. G., "Deposit growth dynamics: particle sticking and scattering phenomena*", J. Powder Tech.*, in press, 1999.

48. Tognotti, L., Longwell J. P. and Sarofim, A. F., *23rd Int. Symp. Comb.*, p.1207, 1990.

49. Cooper B.J., Thoss J.E. "Role of NO in Diesel Particulate Emission Control" *SAE Paper No. 890404*, 1989.

DEFINITIONS, ACRONYMS, ABBREVIATIONS

A: total filtration area
A_o: filtration area of a single channel
b: "unit cell" diameter
$C_{p,1}$: particle layer heat capacity
$C_{p,g}$: gas phase heat capacity
$C_{p,s}$: filter wall heat capacity
d_c: loaded collector diameter
d_{c0}: clean collector diameter
d_p: particle diameter
d_{pore}: pore diameter
D: monolithic trap diameter

D_p: particle diffusion coefficient : $\dfrac{k_B \cdot T}{3\eth \cdot i \cdot d_p} \cdot SCF$

E: grade collection efficiency
E_{cat}: activation energy for catalytic soot oxidation
E_{f1}, E_{f2}, E_{f3}: parameters in CO selectivity Eqs.(A.42)-(A.44)
E_{NO}: activation energy for NO oxidation
E_{NO_2}: activation energy for carbon oxidation by NO_2
E_{num}: total collection efficiency by number
E_{th}: activation energy for thermal carbon oxidation
E_{vol}: total collection efficiency by volume
$f(\varepsilon)$: geometric function by Kuwabara, see Eq. (A.39)
f_{CO}^{the}: thermal CO selectivity for carbon oxidation
f_{CO}^{cat}: catalytic CO selectivity for carbon oxidation
F: factor equal to 28.454
$g(\varepsilon)$: geometric function by Kuwabara, see Eq. (A.27)
g_{CO}: CO selectivity for carbon oxidation by NO_2
k: loaded filter wall permeability
k_0: clean filter wall permeability
k_B: Boltzman's constant 1.38×10^{-23} J/moleÞK
k_{f1}, k_{f2}, k_{f3}: parameters in CO selectivity Eqs. (A.42)-(A.44)
$k_{o,cat}$: frequency factor for catalytic carbon oxidation
$k_{o,th}$: frequency factor for thermal carbon oxidation
$k_{o,NO}$: frequency factor for NO oxidation
k_{o,NO_2}: frequency factor for carbon oxidation with NO_2
k_{soot}: particulate layer permeability
Kn_p: particle Knudsen number, $2\lambda/d_p$
L: effective channel length
$\dot{m}$: exhaust gas mass flow rate
$\dot{m}_p$: particulate mass flow rate per unit collector
m_c: deposited particulate mass per unit collector
m_1: particulate mass in Layer I
$m_{1,0}$: initial particulate mass in Layer I
m_2: particulate mass in Layer II
$m_{2,0}$: initial particulate mass in Layer II
m_b: initial total particulate mass

m_{soot}: particulate mass collected in DPF
m_w: particulate mass in the filter wall
M_c: molecular weight of carbon deposit
M_{NO_2}: molecular weight of NO_2
M_{O_2}: molecular weight of oxygen
MW: gas molecular weight
n: exponent in Eq. (A.47)
N_{cells}: number of inlet cells of wall-flow filter
N_R: interception parameter, Eq. (A.30)
Pe: Peclet number, Eq. (A.24)
Q: exhaust volumetric flow rate
Q_o: exhaust volumetric flow rate of a single channel
R: Universal gas constant
Re: trap entrance Reynolds number, $U\alpha / \nu$
R_j^i: depletion rate of species *j* in Layer *i*
s: interception exponent, Eq. (A.29)
S_p: specific area of deposit layer
T: temperature of the filter wall (used in Appendix IV)
T: gas temperature
T_i: temperature of exhaust gases (used in Appendix IV)
U: inlet channel entrance velocity
U_i: interstitial or pore velocity, Eq. (A.25)
u_w: filter wall/approach velocity
V_{trap}: filter volume
w: particulate layer thickness
w_s: filter wall thickness
x: filter wall thickness coordinate
y_i: mole fraction of species *i* in the exhaust gas
$y_{w,i}$: local mole fraction of species *i* in the wall
Y_i: mass fraction of species *i* in the exhaust gas
$Y_{w,i}$: local mass fraction of species *i* in the wall

Greek letters

α: honeycomb filter cell size
β: particulate-catalyst contact fraction
γ: exponent in Eq. (A.47)
$\Delta H_{NO_2}^{CO}$: specific heat of CO formation (oxidation by NO_2)
$\Delta H_{O_2}^{CO}$: specific heat of CO formation (oxidation by O_2)
$\Delta H_{O_2}^{CO_2}$: specific heat of CO_2 formation (oxidation by O_2)
$\Delta H_{NO_2}^{CO_2}$: specific heat of CO_2 formation (oxidation by NO_2)
ΔP: pressure drop across the filter
ε: loaded filter porosity
ε_0: clean filter porosity
λ: exhaust gas-mean-free-path
μ: exhaust dynamic viscosity
μ_1, μ_2, μ_3: parameters in CO selectivity Eqs. (A.42)-(A.44)
ν: exhaust kinematic viscosity
ξ: interaction parameter between Layers I and II [14, 31]
ρ: exhaust gas density
$\rho_{soot, c}$: particulate packing density in cake deposit
$\rho_{soot, w}$: particulate packing density inside filter wall
ρ_{sub}: bulk density of filter substrate
σ: honeycomb filter cell density
φ: initial soot mass fraction in Layer I
ψ: "unit cell" bridging onset parameter in Eq.(A.38)

LOADED FILTER MODEL

Analytical – The clean filter flow model of Konstandopoulos and Johnson [4] is here extended for high particulate loading effects. The loading is assumed to be uniform across the filter channels since the flow would self-adjust to follow the path of least resistance as the filter gets loaded. This is also supported by separate deposit growth simulations into the filter channels (see also [14]). The basic equation for the pressure drop of a clean wall flow filter is [4,17]:

$$\Delta P_{clean} = \frac{\mu}{k_o} \frac{U\alpha}{4L} w_s + \frac{2\mu F}{3\alpha^2} UL$$
(A1)

where the first term represents losses through the porous walls and the second term frictional losses along the filter channel.

Expressing the channel inlet velocity in terms of the total exhaust gas volume flow Q :

$$U = \frac{8Q}{\pi D^2 \sigma \alpha^2}$$
(A2)

$$\text{where} \quad \sigma = \frac{1}{(\alpha + w_s)^2}$$
(A3)

Eq. (A1) takes the form :

$$\Delta P_{clean} = \frac{\mu Q}{2V_{trap}} (\alpha + w_s)^2 \left[\frac{w_s}{k_o \alpha} + \frac{8FL^2}{3\alpha^4} \right]$$
(A4)

The clean filter model is extended to the arbitrary loaded filter case employing the *ansatz* that the second term of Eq. (A1) can be split as:

$$\Delta P = \underbrace{\frac{\mu}{k_o} \frac{U\alpha}{4L} w}_{wall} + \underbrace{\frac{1\mu F}{3\alpha^2} UL}_{inlet\ channel} + \underbrace{\frac{1\mu F}{3\alpha^2} UL}_{outlet\ channel} =$$

$$= \frac{\mu Q}{2V_{trap}} (\alpha + w_s)^2 \left[\underbrace{\frac{w_s}{k_o \alpha}}_{wall} + \underbrace{\frac{4FL^2}{3\alpha^4}}_{inlet\ channel} + \underbrace{\frac{4FL^2}{3\alpha^4}}_{outlet\ channel} \right]$$
(A5)

and that the splitting remains valid for a loaded filter as well. The pressure drop of a loaded filter then consists of four contributions:

$$\Delta P = \Delta P_{filter\ wall} + \Delta P_{soot\ layer} +$$
$$\Delta P_{inlet\ channel} + \Delta P_{outlet\ channel}$$
(A6)

where the first two components obey Darcy's law and the other two are obtained taking into account the real flow area and its effects on axial velocities (see below Eqs. (A11) and (A12)), separately for each channel.

The first term is given as in Eq. (A4) by:

$$\Delta P_{filter\ wall} = \frac{\mu Q}{2V_{trap}} (\alpha + w_s)^2 \left(\frac{w_s}{k_o \alpha} \right)$$
(A7)

The second term of Eq. (A6) can be evaluated by integrating Darcy's law across the deposit thickness, to account for the variation of the cross sectional flow area, A_o which is significant for high deposit loadings (see Figure A1):

$$\Delta P_{soot\ layer} = \frac{\mu}{k_{soot}} \int_0^w u(x)dx = \frac{\mu}{k_{soot}} \int_o^w \frac{Q_o}{A_o} dx =$$

$$= \frac{\mu Q_o}{4L k_{soot}} \int_0^w \frac{1}{(\alpha - 2w + 2x)} dx =$$

$$= \frac{\mu Q(\alpha + w_s)^2}{L\pi D^2 k_{soot}} ln\left(\frac{\alpha}{\alpha - 2w} \right)$$
(A8)

For a loaded filter the volume of particulate mass deposited in one inlet channel (see Figure A1) is given by:

$$V_{soot} = \frac{m_{soot}}{N_{cells} \rho_{soot,c}} =$$

$$\left[\alpha^2 L - (\alpha - 2w)^2 L \right] = 4\alpha w L \left(1 - \frac{w}{\alpha} \right)$$
(A9)

Re-arranging gives the particulate layer thickness in terms of the deposited mass:

$$w = \frac{\alpha - \sqrt{\alpha^2 - \dfrac{m_{soot}}{N_{cells} L \rho_{soot,c}}}}{2}$$
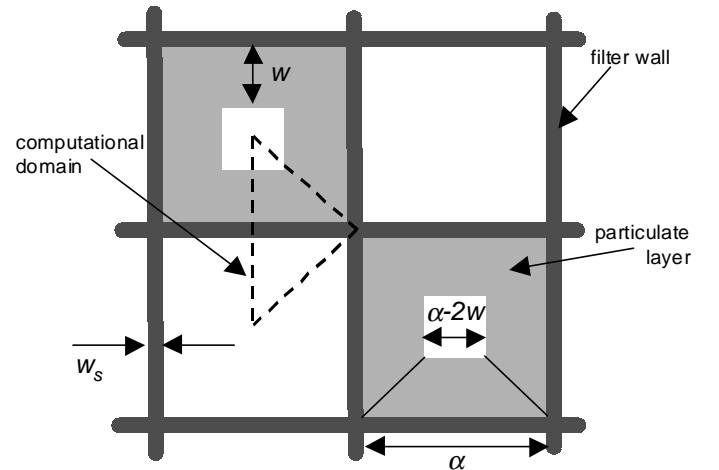(A10)

Figure A1. Cross section of loaded filter channels showing CFD computational domain.

For the inlet (loaded) channel the effective channel width is given by:

$$\alpha^* = \alpha - 2w \tag{A11}$$

resulting in the following value for inlet channel axial velocity:

$$U_I^* = \frac{8Q}{\pi D^2 \sigma (\alpha - 2w)^2} \tag{A12}$$

Applying the previously mentioned *ansatz*, the loaded inlet channel losses are then written from Eq. (A 5), as:

$$\Delta P_{inlet\ channel} = \frac{\mu Q}{2V_{trap}} (\alpha + w_s)^2 \left(\frac{4FL^2}{3(\alpha - 2w)^2} \right) \tag{A13}$$

while the outlet channel losses remain the same as for a clean filter:

$$\Delta P_{outlet\ channel} = \frac{\mu Q}{2V_{trap}} (\alpha + w_s)^2 \left(\frac{4FL^2}{3\alpha^2} \right) \tag{A14}$$

The final equation for the pressure drop is obtained by summing up Eqs. (A7, A8, A13, A14):

$$\Delta P = \frac{\mu Q}{2V_{trap}} (\alpha + w_s)^2 \left[\frac{w_s}{k_o \alpha} + \frac{1}{2k_{soot}} ln \left(\frac{\alpha}{\alpha - 2w} \right) + \frac{4FL^2}{3} \left(\frac{1}{(\alpha - 2w)^4} + \frac{1}{\alpha^4} \right) \right] \tag{A15}$$

The effect of non-Darcian flow in the porous wall can be straightwardly included in the model as shown in [17]. It should be noted though that it is not desirable, from a practical point of view, to operate DPF's in the non Darcian regime, as there is a penalty of increased pressure drop for the same useful filtration area.

Note that in the above derivations the entrance and exit pressure losses due to the contraction and expansion of the flow into and out of the monolith channels have not been taken into account, as their contribution is negligible. This is shown by the following analysis. The pressure drop at the entrance and at the exit are given by [44]:

$$\Delta P_{entrance} = \zeta_E \frac{\rho U^2}{2} \tag{A16}$$

ζ_E is a factor varying from 0.2 to 0.8 according to area blockage ratio and *Re*. The values for these components of the pressure drop are of $O(10^{-2}\text{-}10^{-3})$ compared to the total pressure drop of the loaded filter, hence they are considered negligible.

3-D CFD Validation – To assess the validity of the 1-D analytical model, 3-D CFD simulations were performed on a single channel of a DPF (Table A1), for various particulate loadings. The study was performed using a commercial CFD package [45]. The flow is steady and laminar as the Reynolds number based on the channel width is around 300. Taking advantage of the symmetry of the geometry of the problem, and of the unstructured mesh capabilities of the code, only the triangular section shown in Figure A1 is simulated.

Table A1. Input Data for CFD Simulations

Inlet Velocity U (m/sec)	5.85 – 29.62
Gas density, ρ (kg/m^3)	0.64
Viscosity, μ (kg/m/sec)	2.87x10^{-5}
Wall permeability, k_o (m^2)	5.3x10^{-13}
Deposit permeability (m^2)	3.2x10^{-14}
Channel width, α (mm)	1.44
Channel length, L (mm)	144
Wall thickness, w_s (mm)	0.356
Deposit thickness w (mm)	0.0 – 0.4

The 3-D unstructured grid shown in Figure A2, consists of 105,000 hexahedral cells, with 300 of them distributed along the channel length. Nodes are clustered towards the porous walls to represent better the boundary layer, and towards the inlet and outlet sides to capture the velocity variations. Each CFD simulation point in Figure A4 takes about 100 minutes of CPU time on a Digital 500 series Alphastation with 320 Mb of RAM.
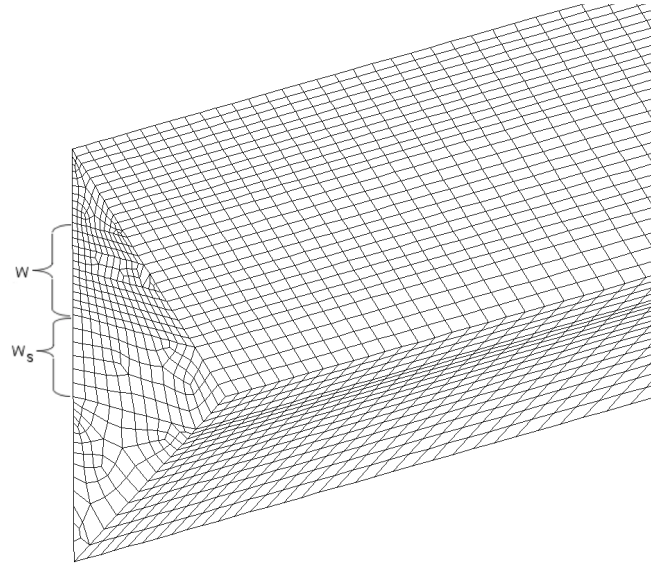

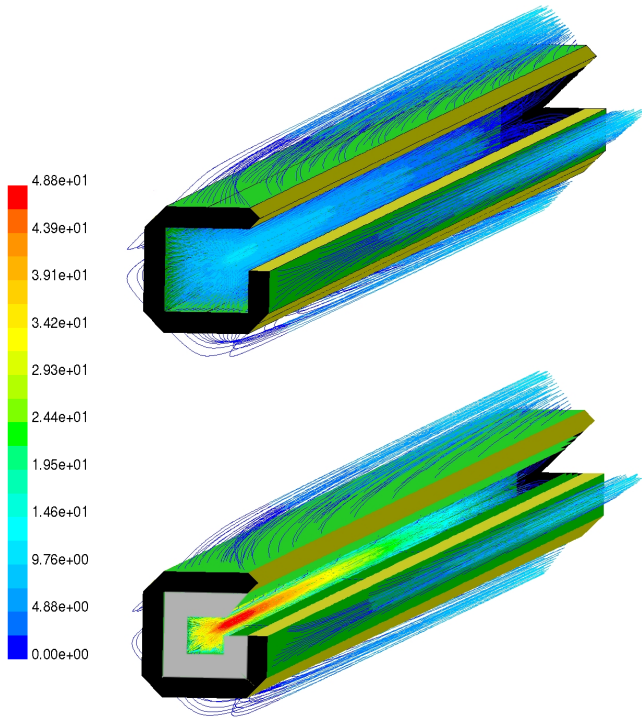Figure A2. Front part of the 105,000 cells unstructured grid.

Figure A3. Streamlines colored by velocity magnitude (m/sec) for a clean (top) and a loaded (bottom) channel of a 5.66"x6" 200 cpi filter.

Figure A3 displays the flow streamlines in the inlet channel of the loaded filter of Figure 4. The streamlines of the clean filter are also shown for comparison.

The contributions of each term of Eq. (A6) are plotted in Figure A4, and are shown to be in very good agreement with the 1-D analytical model.
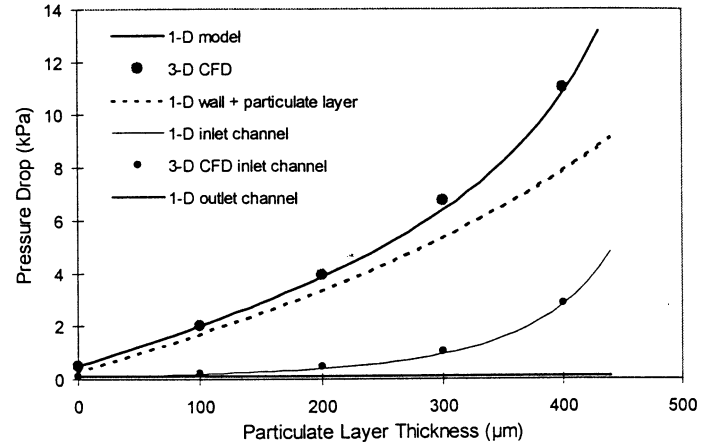

Figure A4. Diagram showing the contributions of the pressure drop as predicted by the analytical model and the CFD simulations.

APPENDIX II

SLIP-FLOW CORRECTION OF PERMEABILITY

When continuum fluid mechanics is applicable, the permeability coefficient entering Darcy's law is an intrinsic property of the porous medium. In this case the influence of temperature on filter pressure drop is due only to the variation of the exhaust gas viscosity and density with temperature. This translates into a power-law dependence of the filter pressure drop on temperature.

When the mean-free-path of the gas molecules approaches the pore size of the porous medium, it is necessary to account for slip and transitional flow effects, which depend on the magnitude of the local Knudsen, Kn number:

$$Kn = \frac{2\lambda}{d_{pore}}$$

(A17)

with the mean-free-path of the gas given by:

$$\lambda = v\sqrt{\frac{\pi MW}{2RT}}$$

(A18)

Exploiting the similar problem for the non-continuum drag of a spherical particle [46] we employ the Stokes-Cunningham Factor (SCF) to correct for slip-flow effects on the permeability:

$$SCF = 1 + Kn\left(1.257 + 0.4e^{-1.1/Kn}\right)$$

(A19)

$$k_{slip\ flow} = SCF \cdot k_{continuum}$$

(A20)

As seen in Figure 2 this approach captures very well the experimental data [20] for a membrane coated filter. In that case the membrane Knudsen number varies from 0.3 to 0.7 as the temperature varies from 20 °C to 400 °C.

APPENDIX III

TRANSIENT FILTRATION MODEL

The transient filtration model is based on applying locally across the filter wall, "unit collector" filtration theory in a self-consistent manner. The filter wall is divided into slabs (Figure A5) and the calculation of the variation of the

local properties ("unit collector" diameter, porosity, permeability etc.) is performed by tracking the amount of particulate mass accumulated in each slab. The "unit collector" model used here, is that of spherical collectors [4,39] since it is closer to the granular structure of extruded ceramic and sintered metal filters. However any

other "unit collector" model can be employed for other filter structures (e.g. fibers).
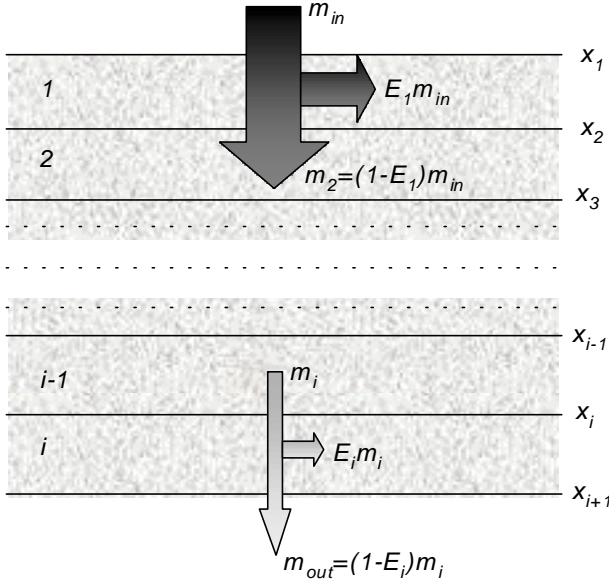

Figure A5. Schematic representation of filter wall discretization into slabs of "unit cell/collectors".

Representing the microstructure of the filter by spherical "unit cells" of size b, each hosting a collector of size d_c, the "unit collector" is assumed to collect particles through the mechanisms of Brownian diffusion and interception [4,39] with combined efficiency denoted by η_{DR}. The collection efficiency E for the clean filter can then be related to η_{DR} by integrating across the filter wall thickness (see [4,39] and references therein):

$$E = 1 - exp\left[-\frac{3\eta_{DR} \cdot (1-\varepsilon_0) \cdot w_s}{2\varepsilon_0 d_{c0}}\right]$$

(A21)

The "unit collector" size is related to the "unit cell" size through the porosity according to:

$$\frac{b^3}{d_{c_0}^3} = (1-\varepsilon_0)$$

(A22)

The single spherical collector efficiency for Brownian diffusion is given by (see [4,39] and references therein):

$$\eta_D = 3.5 \cdot g(\varepsilon) \cdot Pe^{-2/3}$$

(A23)

where the Peclet number is given by:

$$Pe = \frac{U_i \cdot d_c}{D_p}$$

(A24)

and U_i represents the "interstitial" or "pore" velocity related to the approach velocity u_w by :

$$U_i = \frac{u_w}{\varepsilon}$$

(A25)

The unit collector diameter d_{c0} for a clean filter is given by [4,39]:

$$d_{c0} = \frac{3}{2} \cdot \frac{(1-\varepsilon_0)}{\varepsilon_0} \cdot d_{pore}$$

(A26)

and the geometric function $g(\varepsilon)$ for the Kuwabara "unit cell" is [4,39]:

$$g(\varepsilon) = \left[\frac{\varepsilon}{2 - \varepsilon - \frac{9}{5} \cdot (1-\varepsilon)^{1/3} - \frac{1}{5} \cdot (1-\varepsilon)^2}\right]^{1/3}$$

(A27)

while the efficiency due to interception is given by [4,39]:

$$\eta_R = 1.5 \cdot N_R^2 \cdot \frac{[g(\varepsilon)]^3}{(1+N_R)^s}$$

(A28)

with the exponent s defined as :

$$s = \frac{3 - 2\varepsilon}{3\varepsilon}$$

(A29)

and the interception parameter N_R computed as [4,39]:

$$N_R = \frac{d_p}{d_c}$$

(A30)

Assuming the two collection mechanisms to be independent of each other, the combined collection efficiency η_{DR} can be expressed as [4,39]:

$$\eta_{DR} = \eta_D + \eta_R - \eta_D \cdot \eta_R$$

(A31)

The particulate mass deposited in the filter m_c satisfies:

$$\frac{\partial \dot{m}_p}{\partial x} + \frac{\partial m_c}{\partial t} = 0$$

(A32)

$$\frac{\partial \dot{m}_p}{\partial x} = -e_f(m_c)\dot{m}_p$$

(A33)

The above hyperbolic system is solved numerically by discretizing the filter depth into slabs as shown in Figure A5. As mass enters the filter, it is distributed in it according to the local collection efficiency in each slab E_i.

The mass deposited at each slab is modifying the local "unit collector" size according to:

$$d_c(i,t) = 2 \cdot \left[\frac{3}{4\pi} \cdot \frac{m_c(i,t)}{\rho_{soot,w}} + \left(\frac{d_{c_0}}{2}\right)^3\right]^{1/3}$$

(A34)

Respectively the local porosity ε of the filter as a function of time is given by:

$$\varepsilon(i,t) = 1 - \left(\frac{d_c(i,t)}{d_{c_0}}\right)^3 \cdot (1-\varepsilon_0)$$

(A35)

and the slab collection efficiency evolution $E(i,t)$ is computed from:

$$E(i,t) = \int_{x_i}^{x_{i+1}} e_f(m_c(x,t))dx =$$

$$1 - exp\left[-\frac{3\eta_{DR}(i,t)\cdot(1-\varepsilon(i,t))\cdot(x_{i+1}-x_i)}{2\varepsilon(i,t)d_c(i,t)} \right] \quad (A36)$$

The particles are collected initially inside the filter wall but eventually, they form a cake on its frontal area. It is therefore useful to define a partition coefficient Φ ($0\leq\Phi\leq1$) that determines the fraction of mass collected in the first slab that contributes to cake formation. Based on geometrical grounds this partition coefficient is expected to depend on the dimensionless blocked-area fraction at the scale of the unit "collector". Φ is assumed to be given by :

$$\Phi(t) = \left(\frac{(d_c(1,t))^2 - d_{c_0}^2}{(\psi \cdot b)^2 - d_{c_0}^2} \right) \quad (A37)$$

where ψ is a dimensionless "percolation" control constant ($0<\psi<1$), that determines the onset of pore bridging, which has to be estimated from experimental data or detailed discrete particle dynamics simulations using the methods of [47].

The local permeability of the filter wall changes as the particles deposit on each "unit collector". The local permeability k_i of the loaded filter is related to the permeability of the clean filter k_0 by:

$$\frac{k(i,t)}{k_0} = \left(\frac{d_c(i,t)}{d_{c_0}} \right)^2 \cdot \frac{f(\varepsilon(i,t))}{f(\varepsilon_0)} \quad (A38)$$

where $f(\varepsilon)$ is a geometric function defined as follows for the Kuwabara "unit cell" [4,39]:

$$f(\varepsilon) = \frac{2}{9} \cdot \frac{\left[2 - \frac{9}{5}\cdot(1-\varepsilon)^{1/3} - \varepsilon - \frac{1}{5}\cdot(1-\varepsilon)^2 \right]}{(1-\varepsilon)} \quad (A39)$$

APPENDIX IV

NO$_2$ SOOT OXIDATION

In this Appendix the incorporation of NO$_2$-assisted particulate oxidation into the regeneration model framework of Konstandopoulos and Kostoglou [14, 31, 32] is performed.
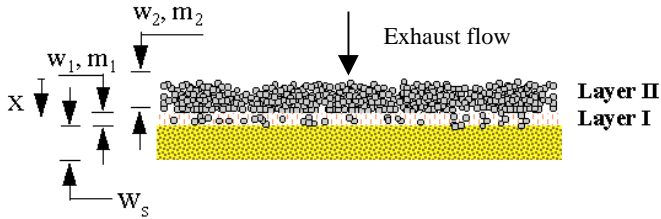

Figure A6. Schematic illustrating the filter wall, catalytic coating influenced Layer I and overlaid particulate deposit Layer II.

With reference to Figure A6, exhaust gases pass perpendicular to the wall of the filter with a specified mass flux imposed by the exhaust flow rate (which in general is time dependent), $\dot{m}(t)$ and the total filtration area of the filter, A, satisfying the following balance equation :

$$\frac{d}{dx}(\rho u_w) = 0 \quad (A40)$$

which upon integration along the particle/wall layer (Figure A6) becomes:

$$\rho u_w = \frac{\dot{m}}{A} \quad (A41)$$

For analytic simplicity, particulate oxidation [see Eqs. (2), (3)] is assumed to follow a first-order heterogeneous oxidation both in the presence and absence of catalyst but with, in principle, different reaction CO selectivity for the non-catalyst and catalyst influenced reactions, denoted as f_{CO}^{the} and f_{CO}^{cat} respectively, and assumed to have a temperature dependence of the following form [48]:

$$f_{CO}^{the} = \frac{1}{1 + k_{f1}\, y_{O_2}^{\mu_1}\, e^{E_{f1}/RT}} \quad (A42)$$

$$f_{CO}^{cat} = \frac{1}{1 + k_{f2}\, y_{O_2}^{\mu_2}\, e^{E_{f2}/RT}} \quad (A43)$$

The CO selectivity g_{CO} for the first-order [49] oxidation reaction of soot by NO$_2$, is assumed to have also a similar to Eqs. (A42)-(A43) temperature dependence:

$$g_{CO} = \frac{1}{1 + k_{f3}\, y_{O_2}^{\mu_3}\, e^{E_{f3}/RT}} \quad (A44)$$

The oxygen and NO$_2$ balance equations in terms of the local oxygen mass fraction Y_{w,O_2} and local NO$_2$ mass fraction Y_{w,NO_2} for each layer can then be written as follows:

Layer II – In this layer soot oxidation with oxygen occurs only through the non-catalytic path.

O_2 mass balance

$$\frac{d}{dx}(\rho u_w Y_{w,O_2}) = -S_p \rho Y_{w,O_2} k_{th}(T)(1 - f_{CO}^{the}/2)$$

(A45)

NO_2 mass balance

$$\frac{d}{dx}(\rho u_w Y_{w,NO_2}) = -S_p \rho Y_{w,NO_2} k_{NO_2}(T)(2 - g_{CO})$$

(A46)

Layer I – In this layer occurs additional production of NO_2 from NO and O_2. A general kinetic expression is assumed for this reaction (see [49] for the reaction orders):

$$\frac{dy_{NO_2}}{dt} = k_{NO} y_{O_2}^\gamma y_{NO}^n$$

(A47)

with an Arrhenius form for the rate constant:

$$k_{NO}(T) = k_{o,NO} e^{-(\frac{E_{NO}}{RT})}$$

(A48)

O_2 mass balance

$$\frac{d}{dx}(\rho u_w Y_{w,NO_2}) = -S_p \rho Y_{w,O_2} \times$$

$$[(1 - \beta)k_{th}(T)(1 - f_{CO}^{the}/2) + \beta k_{th}(T)(1 - f_{CO}^{the}/2)]$$

$$- \frac{1}{2} \frac{k_{NO}(T)}{M_{O_2}} y_{w,NO}^n y_{w,O_2}^\gamma$$

(A49)

NO_2 mass balance

$$\frac{d}{dx}(\rho u_w Y_{w,NO_2}) = -S_p \rho Y_{w,NO_2} \times$$

$$k_{NO_2}(T)(2 - g_{CO}) + \frac{k_{NO}(T)}{M_{NO_2}} y_{w,NO}^n y_{w,NO_2}^\gamma$$

(A50)

The local NO mole fraction $y_{w,NO}$ is obtained from the total nitrogen atoms conservation:

$$y_{w,NO} = y_{NO} + y_{NO_2} - y_{w,NO_2}$$

(A51)

In Eq. (A49) it has been assumed that inside the catalytically affected layer, carbon oxidation proceeds according to two paths, a catalytic path over a certain fraction of the carbon specific area, β and a non-catalytic (thermal) path over the rest. This is the simplest way to account for the effect of incomplete contact between particles and catalytic sites. Each path has in principle its own activation energy and frequency factor assumed to be given by a modified-Arrhenius form [14, 30]:

$$k_{th}(T) = k_{o,th} T e^{-(\frac{E_{th}}{RT})}$$

(A52)

$$k_{cat}(T) = k_{o,cat} T e^{-(\frac{E_{cat}}{RT})}$$

(A53)

The rate constant for carbon oxidation by NO_2 is assumed to have an Arrhenius form:

$$k_{NO_2}(T) = k_{o,NO_2} e^{-(\frac{E_{NO_2}}{RT})}$$

(A54)

The exhaust gas density is related to temperature via the ideal gas law. Upon integration across the respective layer thicknesses the total rate of oxygen and NO_2 depletion per layer can be derived as shown below. In Layer I we distinguish between oxygen depleted in the non-catalytic and catalytic paths:

O_2 and NO_2 depletion rates

$$R_{O_2}^{II} = \rho u_w Y_{O_2} (1 - e^{\frac{-S_p k_{th}(T)(1 - f_{CO}^{the}/2)w_2}{u_w}})$$

(A55)

$$R_{NO_2}^{II} = \rho u_w Y_{NO_2} (1 - e^{\frac{-S_p k_{NO_2}(T)(1 - f_{CO}^{the}/2)w_2}{u_w}})$$

(A56)

$$R_{O_2}^{I,th} = \rho S_p(1 - \beta)k_{th}(T)(1 - f_{CO}^{the}/2) \int_{w_2}^{w_1+w_2} Y_{w,O_2} dx$$

(A57)

$$R_{O_2}^{I,cat} = \rho S_p \beta k_{th}(T)(1 - f_{CO}^{cat}/2) \int_{w_2}^{w_1+w_2} Y_{w,O_2} dx$$

(A58)

$$R_{NO_2}^I = \rho S_p k_{NO_2}(T)(2 - g_{CO}) \int_{w_2}^{w_1+w_2} Y_{w,NO_2} dx$$

(A59)

Introducing the following decompositions of the total particulate mass m_{soot} and layer thickness w (where the subscript 0 denotes initial conditions):

$$m_{soot} = m_1 + m_2$$
$$m_{1,0} = \phi m_b$$
$$m_{2,0} = (1 - \phi)m_b$$

(A60)

$$w = w_1 + w_2$$

(A61)

and invoking a quasi-steady approximation for the rate of particulate deposit depletion, we can write the following evolution equations for the particulate mass in each layer:

$$\frac{1}{A}\frac{dm_1}{dt} = -(1 - \xi)(\frac{M_c}{M_{O_2}} \frac{1}{1 - f_{CO}^{the}/2} R_{O_2}^{I,th} +$$

$$\frac{M_c}{M_{O_2}} \frac{1}{1 - f_{CO}^{cat}/2} R_{O_2}^{I,cat} + \frac{M_c}{M_{NO_2}} \frac{1}{2 - g_{CO}} R_{NO_2}^I)$$

(A62)

$$\frac{1}{A}\frac{dm_2}{dt} = -(\frac{M_c}{M_{O_2}} \frac{1}{1 - f_{CO}^{the}/2} R_{O_2}^{II} +$$

$$\frac{M_c}{M_{NO_2}} \frac{1}{2 - g_{CO}} R_{NO_2}^{II})$$

$$- \xi(\frac{M_c}{M_{O_2}} \frac{1}{1 - f_{CO}^{the}/2} R_{O_2}^{I,th} +$$

$$\frac{M_c}{M_{O_2}} \frac{1}{1 - f_{CO}^{cat}/2} R_{O_2}^{I,cat} + \frac{M_c}{M_{NO_2}} \frac{1}{2 - g_{CO}} R_{NO_2}^I)$$

(A63)

In writing these equations we have introduced a "mixing parameter", x to account for the interaction between the two layers [14]. In the above developments we have assumed that regeneration occurs so fast, that it is permissible to assume that no further deposit growth happens as the soot laden, exhaust gases pass through the filter. It is straightforward though to include a particulate deposit growth term on the right hand side of Eq. (A63), see [14].

Applying a small-Peclet number perturbation expansion similar to that in [29, 30] we find that the filter temperature evolution is given by:

$$\frac{dT}{dt} = \frac{\dot{m}c_{pg}}{(\rho_{soot}c_{p1}w + \rho_{sub}c_{ps}w_s)}(\frac{A}{\dot{m}c_{pg}}Q_r + T_i - T)$$

(A64)

where $T_i(t)$ is the filter inlet temperature (in general a function of engine operating point, hence time).

The oxidation reactions Eqs.(2)-(4) generate heat that is given by:

$$Q_r = [\Delta H_{O_2}^{CO} f_{CO}^{the} + \Delta H_{O_2}^{CO_2}(1 - f_{CO}^{the})] \times$$

$$\frac{R_{O_2}^{I,th} + R_{O_2}^{II}}{M_{O_2}(1 - f_{CO}^{the}/2)} + [\Delta H_{O_2}^{CO} f_{CO}^{cat} +$$

$$\Delta H_{O_2}^{CO_2}(1 - f_{CO}^{cat})]\frac{R_{O_2}^{I,cat}}{M_{O_2}(1 - f_{CO}^{cat}/2)} +$$

$$[\Delta H_{NO_2}^{CO} g_{CO} + \Delta H_{NO_2}^{CO_2}(1 - g_{CO})] \times$$

$$\frac{R_{NO_2}^{I} + R_{NO_2}^{II}}{M_{NO_2}(2 - g_{CO})} +$$

(A65)

where the respective heats of reaction have been computed based on the stoichiometry of the reactions, accounting for finite CO selectivity.

The mass balances in Layer II are integrated analytically to give the depletion rates in Eqs. (A55) and (A56) and the initial conditions for the integration of mass balances in Layer I

At $x=w_2$ we find:

$$Y_{w,O_2} = Y_{O_2}(1 - e^{\frac{-S_p k_{th}(T)(1 - f_{CO}^{the}/2)w_2}{u_w}})$$

(A66)

$$Y_{w,NO_2} = Y_{NO_2}(1 - e^{\frac{-S_p k_{NO_2}(T)(1 - f_{CO}^{the}/2)w_2}{u_w}})$$

(A67)

The mass balances in Layer I cannot be integrated analytically. Eqs. (A57)-(A59) are differentiated with respect to x and are combined with Eqs. (A49)-(A50) to form a system of 5 ODE's in the spatial domain. This system is solved with an explicit Runge-Kutta method with constant step (spatial integration). For the time integration of Eqs. (A62) and (A63) an explicit integrator with prespecified accuracy and automatically adapted step is used [28]. Results from application of the model are shown in Figures 20-22.